Study of Behaviors of Multi-Source Rauch Filters

MinhTri Tran*, Anna Kuwana, Haruo Kobayashi

Division of Electronics and Informatics, Gunma University, Kiryu 376-8515, Japan
* trantri.ks@gmail.com; kuwana.anna@gunma-u.ac.jp; koba@gunma-u.ac.jp

***Abstract*— This paper presents a study of behaviors of high-order multi-source Rauch filters based on the characteristics of complex functions. The advantages of Rauch's connections are an easier selection of circuit components and a simpler design in fully differential forms and complex topologies. A general superposition formula is also introduced for deriving the transfer functions of multi-source transmission networks such as fully differential amplifiers, fully differential low-pass filters, polyphase filters, complex filters, and quadrature signal generation circuits because the shapes of any motions and the characteristics of any transmission networks are analyzed based on superposition principle. The proposed Nichols chart of the self-loop function is used to do the ringing test for high-order Rauch low-pass filters because it can be easily calculated using MATLAB, simulated using SPICE, and measured in Network Analyzers. The innovation of Nichols chart of self-loop function is a useful tool for the ringing test for high-order networks. The simulation results of the phase margin at unity gain of the self-loop function in a proposed design of the 4th-order Rauch low-pass filter are 74 degrees (over-damping region), 68 degrees (critical damping region), and 59 degrees (under-damping region). The pass-band gain and the image rejection ratio of the proposed design of a 4th-order Rauch complex filter are 12 dB and 32 dB, respectively. It's shown that complex functions play an important role in mathematical models of motion in the multi-source networks.**

Keywords*— *Ringing Test, Self-Loop Function, Nichols Chart, Rauch Filter, Multi-Source Network, Superposition Principle.

I. Introduction

Modeling of motion is one of the most important topics in physical science because everything in the universe moves (such as electrons, protons, photons, people, stars, galaxies, and so on…). Complex functions which imaginary unit j represents a 90-degree phase shift are used to describe the shapes of the natural motion in both two-dimensional and three-dimensional domains which are investigated in both time domain and frequency domain. In theoretical analysis and practical measurement, the characteristics of the natural waveforms and the real behaviors of their transmission networks are usually projected in a specific referent complex plain which is investigated at time variation or at frequency variation . In addition, sinusoidal signals are the projections of helix waves on a normal plain. Therefore, helix waves are proposed to analyze the behaviors of analogue signals such as sinusoidal signals, multi-harmonic signals, multi-phase signals in both time and frequency domains [1].

Rauch filters as a class of multi-feedback filters are popular and applied in modern electronics. These filters are often compared with Sallen-Key filters [2]. The motivation of this study on high-order multi-source Rauch filters based on complex functions comes from the high quality of the performance requirements of high-order systems. The conventional concept of loop gain is used to do the stability test in many research papers, textbooks, and commercial products because ringing is a wasteful power. However, the theoretical calculation, the laboratory simulation and the practical measurement of loop gain are not unique, so it is not used to investigate the operating regions of high-order systems. The observation of the phase margin at unity gain of the self-loop function helps us determine the operating regions of high-order systems quickly. With the proposed superposition formula, the transfer functions of high-order complex filters and polyphase filters are easily derived and investigated in both positive and negative frequency domains. The behaviors of multi-source networks are clarified by the theoretical analysis, the laboratory simulations, and the practical measurements.

The main contributions of this work are the analysis of helix waves, the ringing test for a 4th-order fully differential Rauch low-pass filter and the derivation of the transfer function and the image rejection ratio of a 4th-order Rauch complex filter. The proposed Rauch complex filter overcomes some limitations of the conventional filters such as high power-loss in case of high-order RC polyphase filters, and large power-consumptions in case of high-order complex filters. Helix waves are considered as fundamental waveforms of the natural motion. In addition, the use of the superposition formula is a fast network analysis method for high-order multi-source systems.

This paper contains 7 sections. Some basic concepts for modelling of motion are presented in Section II. The classification of the analogue signals is presented in Section III. Section IV shows the proposed superposition formula for deriving the transfer functions of the multi-source systems. The ringing test for high-order Rauch low-pass filters is performed in Section V. The behaviors of a 4th-order Rauch complex filter are investigated in Section VI. The main points of this work are summarized in Section VII.

II. Basic Concepts For Modeling Of Motion

A. Roles of motion models

This section will recall the roles of mathematical models of motion in physical sciences. The state of the object is usually investigated using Cartesian coordinate systems in both two-dimension and three-dimension domains. The shapes of objects are often projected from a referent three-dimension to a referent two-dimension domain. However, the Cartesian coordinate systems are not widely used in the mathematical models of motion because it is very difficult to express the shapes of motion of a natural signal using a pair of numerical coordinates, or a triplet of numerical coordinates at time variation. Therefore, the study of complex numbers in a referent plane continues and has been enhanced in many centuries [3].

A set of complex numbers is also called a complex function which describes the shape of a motion at time variation or the behaviour of a transmission network at frequency variation [4]. It is also known that complex

Copyright © AJSE Publishers

functions arise for a wide variety of reasons and are studied because they may be physically significant and hence cannot be neglected in mathematical models of motion in both time and frequency domains and in both two-dimensional and three-dimensional domains [5]. Moreover, the waveform of a natural motion is often expressed in three-dimension domain. For instance, the shape of a water drop from a faucet in three-dimension domain is given in (1). The waveform of the water drop is shown in Fig. 1.

$$V(t)=\left\{\mathrm{Re}(t)=t\cos(t);\mathrm{Im}(t)=t\sin(t);Al(t)=-\frac{10}{2\sqrt{t}}\sin(t)\right\} \quad (1)$$

The quantitative tools and concepts needed to understand the physical nature of motion in multi-source networks are challenging. It is difficult to investigate the characteristics of a real motion of multi-source networks in both theoretical analysis and practical measurement because the basic theories for large-scale systems are not widely studied [6]. Therefore, the behaviours of a real motion are usually investigated in two-dimensional domain where the shape of waveforms and characteristics of transmission networks are projected in the specific referent complex plains and observed at time variation or at frequency variation [7].

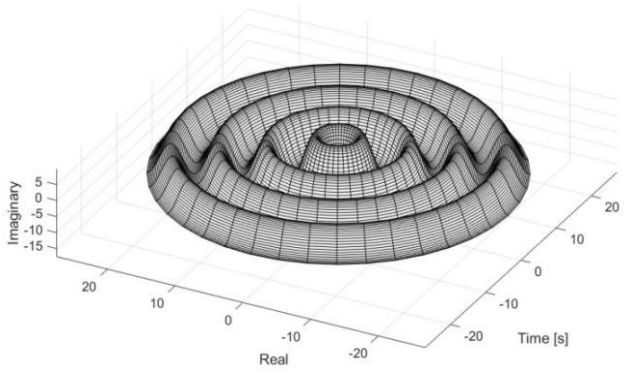


Fig. 1. Waveform of a water drop in a three-dimensional domain.

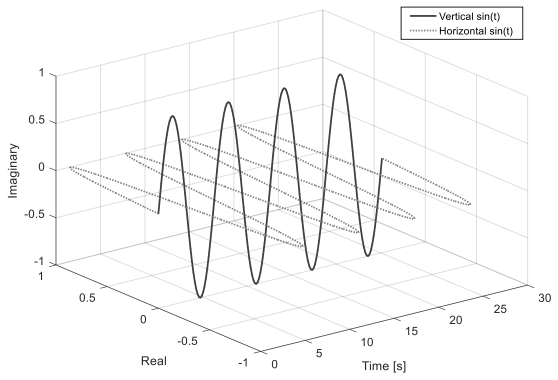


Fig. 2. Shapes of sin(t) and jsin(t) on the vertical and horizontal planes.

B. Meaning imaginary unit in complex numbers

The meaning of imaginary unit in two-dimensional and three-dimensional domains is explained in this section. Complex numbers can be efficiently used for the solutions of polynomial equations because it holds all of the other numbers such as real numbers, rational numbers, and irrational numbers. Although the basic concepts of complex numbers are well known in a simplest equation $x^2 + 1 = 0$, the meaning of imaginary unit j and its applications might not be understood [8].

It's well known that Euler's formula is a mathematical formula in complex analysis that establishes the fundamental relationship between the trigonometric functions and the complex exponential function. Euler's formula is ubiquitous in mathematics, physics, and engineering because Euler's formula evaluates to $e^{j\pi} + 1 = 0$. It is very easy to proof this formula using a power series for sine function ($A\sin(\omega_0 t+ \Theta_0)$) and cosine function ($A\cos(\omega_0 t+ \Theta_0)$) at a specific time in (2). However, it is very difficult to clarify the differences of signal spectrum and system spectrum using Euler's formula or a power series of a complex number because the time and frequency domains of a system are analysed separately [9]. In other words, the waveform and spectrum in time and frequency domains are not well defined in the Euler's formula. Moreover, sinusoidal waves are the shapes of the natural periodic motions which are projected on a referent plane [10]. Therefore, the Euler's formula is not used in the mathematical model of motion because sine and cosine waves on two different planes cannot be added.

$$\begin{aligned}
e^{\theta} &= 1+\frac{\theta}{1!}+\frac{\theta^2}{2!}+\frac{\theta^3}{3!}+\frac{\theta^4}{4!}+\ldots=\sum_{n=0}^{\infty}\frac{\theta^n}{n!}\\
\cos(\theta) &= 1-\frac{\theta^2}{2!}+\frac{\theta^4}{4!}-\frac{\theta^6}{6!}+\ldots=\sum_{n=0}^{\infty}\frac{(-1)^n\theta^{2n}}{(2n)!}\\
\sin(\theta) &= \theta-\frac{\theta^3}{3!}+\frac{\theta^5}{5!}-\frac{\theta^7}{7!}+\ldots=\sum_{n=0}^{\infty}\frac{(-1)^n\theta^{2n+1}}{(2n+1)!}\\
e^{j\theta} &= \sum_{n=0}^{\infty}\frac{(-1)^n\theta^{2n}}{(2n)!}+j\sum_{n=0}^{\infty}\frac{(-1)^n\theta^{2n+1}}{(2n+1)!}=\cos(\theta)+j\sin(\theta)
\end{aligned} \quad (2)$$

For example, the sine functions $V_1(t) = A\sin(\omega_0 t+ \Theta_0)$ and $V_2(t) = jA\sin(\omega_0 t+ \Theta_0)$ where the amplitude is one (A=1), the angular frequency ω_0 is one ($\omega_0=2\pi f_0=1$), and the original phase is zero ($\Theta_0 = 0$) on the horizontal and vertical planes (or real and imaginary planes) are given in (3). Fig. 2 shows the waveforms of two sinusoidal functions $V_1(t)=\sin(t)$ and $V_2(t)=j\sin(t)$ on the vertical and horizontal planes at time variation.

$$\begin{aligned}
V_1(t) &= \left\{\mathrm{Re}(t)=\sin(t);\mathrm{Im}(t)=0;Al(t)=t\right\}\\
V_2(t) &= \left\{\mathrm{Re}(t)=0;\mathrm{Im}(t)=\sin(t);Al(t)=t\right\}
\end{aligned} \quad (3)$$

There are three main factors that set up a model of motion including signal source, transmission network, and time [11]. In time domain, signal sources can be periodic signals (sinusoidal waves, square waves, and so on…), or non-periodic signals. The spectra of signal sources are analysed in frequency domain. Moreover, signal sources can be divided into the single-phase source and the multi-phase source according to the single-ended network and the multi-source network. The transmission network will affect the phase and the amplitude of the signal source in different ways. Transmission networks are usually analyzed in frequency domain. Complex functions are used to express both signal sources and transmission networks. Imaginary unit j represents the 90-degree phase shift from a referent

Copyright © AJSE Publishers

axis in two-dimension domain, or a referent plane in three-dimension domain [12].

In mathematical models of signal sources, complex functions can be expressed in both time and frequency domains. Sine and cosine waves are the shapes of helix waves in different planes. The amplitude in time domain and the magnitude in frequency domain of a sinusoidal signal are not the same. The phase-order of multi-phase signals determines the polarity of complex signals which are called positive and negative polyphase signals [13]. Up to now, the fundamental concepts of helix waves, single-ended signals, complex signals, and polyphase signals are not well defined in both time and frequency domains. In addition, multi-source transmission networks are widely used in wireless communication systems such as fully differential amplifiers, fully differential low-pass filters, polyphase filters, complex filters, and quadrature signal generation circuits while a general stability test for high-order multi-source systems, and a superposition formula for deriving the transfer functions and the image rejection ratios of multi-phase systems are still not introduced [14].

C. Limitations of conventional complex functions analysis

There are some limitations of the conventional methods such as ordinary differential equations, superposition theorem, Nyquist stability condition. Ordinary differential equations are used in many mathematical models of motions [15]. Based on Euler's formula, a second-order ordinary differential equation can be solved easily. In addition, Fourier's transforms, Laplace's transforms, and Hilbert's transforms can be also used to analyse some differential equations of some basic multi-source mechatronic networks in the frequency domain. However, the inability to explicitly solve high-order differential equations arises in elementary courses. One frequently gets the impression that these equations can usually be solved that explicit formulas for the solutions can usually be found in terms of powers, exponentials, and trigonometric functions which are complex functions. Therefore, mathematical models for energy propagations of objects based on complex functions are studied many recent decades [16].

In mathematical models of transmission networks, complex functions can be plotted in Nyquist diagram, Bode plot, and Nichols chart. Kirchhoff's laws lead to the conventional superposition principle for mathematical modeling that describe the relationship between the input and output of electronic systems [17]. However, it takes several times to analyze the behaviors of multi-source networks because the effects of each source should be considered independently. It requires that some signal sources should be removed and replaced without affecting the final result. The application of the conventional superposition principle becomes a painful experience when a high-order multi-phase network is analyzed because it requires a huge amount of hand calculation [18]. Therefore, a superposition formula is introduced for deriving the transfer functions and the image rejection ratios in these multi-phase networks.

In high-order electronic feedback and non-feedback systems, ringing or overshoot voltage causes extra current to flow, which leads to thereby wasting energy, causing extra heating of the components, and making the system unstable [19]. Ringing occurs in both passive and active circuits, and it happens in both feedback and non-feedback systems. Ringing makes the feedback systems unstable. Therefore, the stability test should be done. The stability test is a valuable tool for analyzing high-order systems. Learners, however, often find this topic confusing and difficult to understand [20]. Some reasons for this difficulty and confusion are the derivation of the loop gain in feedback systems and the assumptions of the feedback analysis [21]. Furthermore, it is difficult to analyze the response of overshoot and undershoot of a high-order network, because the corresponding inverse Laplace transform of the response is difficult to compute analytically [22].

The Nyquist diagram of loop gain cannot be applied for high-order linear electronic systems because Nyquist's stability condition does not show the operating regions of a linear network. Moreover, the Nichols chart of loop gain is only used in MATLAB simulation. And, it is not widely used in practical measurements. As a result, Nichols chart of the self-loop function is used to study the operating regions and compute the phase margins of high-order multi-source systems [23]. The inspection of the Nichols chart allows the determination of the exact values of the phase margin at unity gain of the self-loop function in a transfer function. Hence, there is no need to use the Nyquist criterion which is an important stability test with applications to adaptive feedback systems. Furthermore, the phase margin allows the prediction of ringing that drives the system unstable. Therefore, the investigation of phase margin at unity gain of the self-loop function has been the focal point of many extensive research works [24].

III. Classification Of Analogue Signals

A. Behaviors of helix waves

In this section, the properties of helix waves are presented. The sine and cosine waves are the projections of the helix waves on different reference planes. Helix waves are the fundamental waveforms in mathematical models of motion [25]. The patterns of motion in the coil (or inductor), spring pendulum are helix waves. In general, helix waves can be used to express the behaviours of a periodic motion at time variation. The polarity of a helix wave is conventionally determined based on the direction of motion in the transmission network. In the anti-clockwise direction, a positive helix function $V_{he+}(t)$ is written in (4). A positive helix function $V_{he+}(t) = Ahe(\omega_0 t+\Theta_0)$ can be expressed separately in three axis functions: real function $Re(t) = V_{cos+}(t) = A\cos(\omega_0 t+\Theta_0)$, imaginary function $Im(t) = V_{sin+}(t) = A\sin(\omega_0 t+\Theta_0)$, and altitude function $Al(t)=t$. Here, the amplitude is A and the positive rotation angle function is $\Theta_p(t) = \omega_0 t+\Theta_0$. Fig. 3 shows the positive helix function $V_{he+}(t) = he(t)$ at a specific angular frequency ($\omega_0 = 2\pi f_0 = 1$) on the complex plane at time variation. The spectrum of the positive helix wave is given in (5).

$$V_{he+}(t) = Ahe(\omega_0 t+\theta_0) = \begin{cases} \mathrm{Re}(t) = A\cos(\omega_0 t+\theta_0) \\ \mathrm{Im}(t) = A\sin(\omega_0 t+\theta_0) \\ Al(t) = t \end{cases} \quad (4)$$

$$\left|V_{he+}(T_0)\right| = \left|Ahe(\omega_0 T_0+\theta_0)\right| = A\sqrt{2}e^{j(\omega_0 T_0+\theta_0)} \quad (5)$$

In the clockwise direction, a general negative helix function $V_{he-}(t)$ is written in (6). The negative helix function $V_{he-}(t)$ in three separated axis functions are real function

$\mathrm{Re}(t)=V_{cos\text{-}}(t) = A\cos(-\omega_0 t-\Theta_0)$, imaginary function $\mathrm{Im}(t) = V_{sin\text{-}}(t) = A\sin(-\omega_0 t-\Theta_0)$, and altitude function $\mathrm{Al}(t)=t$. Here, the negative rotation angle function is $\Theta_n(t)=-\omega_0 t-\Theta_0$. Fig. 4 shows the negative helix function $V_{he\text{-}}(t) = he(-t)$ at the specific angular frequency ($\omega_0=2\pi f_0=1$) on the complex plane. The spectrum of the negative helix wave is given in (7). In the time domain, the amplitudes and the phases of helix, cosine and sine waves are the same. However, the amplitude in time domain and the magnitude in frequency domain of these waves are not the same.

$$V_{he-}(t) = Ahe(-\omega_0 t-\theta_0)=\begin{cases}\mathrm{Re}(t)=A\cos(-\omega_0 t-\theta_0)\\ \mathrm{Im}(t)=A\sin(-\omega_0 t-\theta_0)\\ Al(t)=t\end{cases} \quad (6)$$

$$\left|V_{he-}(T_0)\right| = \left|Ahe(-\omega_0 T_0-\theta_0)\right| = A\sqrt{2}e^{-j(\omega_0 T_0+\theta_0)} \quad (7)$$

As the amplitude of a helix wave is one, its spectrum is a square root of two. On the contrary, the spectrum of a sine wave is a half of a square root of two when its amplitude is one. The spectra of helix and sine waves are shown in Fig. 5. In addition, the impedances of transmission networks may change the amplitude and phase of signal sources at different frequencies. Therefore, the behaviours of transmission networks are usually analysed in frequency domain. Understanding of helix functions is being able to think flexibly the properties of natural waves in both two-dimensional and three-dimensional domains. Figs. 3, 4, and 5 clearly demonstrate the differences between the amplitude in time domain and the magnitude in frequency domain of helix waves and sinusoidal waves.

In a referent normal plane, waveforms can be divided into single-ended signals, multi-harmonic signals, and multi-phase signals. In a single-ended system, the sinusoidal functions and their spectra are easily derived based on the properties of helix waves. The wave functions and the spectra of sine and cosine waves are given in (8)-(11).

$$\begin{aligned}V_{\cos}(t) &= A\cos(\omega_0 t+\theta_0)=\mathrm{Re}\{V_{he+}(t)\}=\mathrm{Re}\{V_{he-}(t)\}\\ &=\frac{1}{2}\left(\mathrm{Re}\{V_{he+}(t)\}+\mathrm{Re}\{V_{he-}(t)\}\right)\end{aligned} \quad (8)$$

$$\begin{aligned}\left|V_{\cos}(T_0)\right| &= \left|A\cos(\omega_0 T_0+\theta_0)\right|\\ &=\frac{A\sqrt{2}}{2}\left(e^{j(\omega_0 T_0+\theta_0)}+e^{-j(\omega_0 T_0+\theta_0)}\right)\end{aligned} \quad (9)$$

$$\begin{aligned}V_{\sin}(t) &= A\sin(\omega_0 t+\theta_0)=\mathrm{Im}\{V_{he+}(t)\}=-\mathrm{Im}\{V_{he-}(t)\}\\ &=\frac{1}{2}\left(\mathrm{Im}\{V_{he+}(t)\}-\mathrm{Im}\{V_{he+}(t)\}\right)\end{aligned} \quad (10)$$

$$\begin{aligned}\left|V_{\sin}(T_0)\right| &= \left|A\sin(\omega_0 T_0+\theta_0)\right|\\ &=\frac{A\sqrt{2}}{2}\left(e^{j\left(\omega_0 T_0+\theta_0+\frac{\pi}{2}\right)}+e^{-j\left(\omega_0 T_0+\theta_0+\frac{\pi}{2}\right)}\right)\end{aligned} \quad (11)$$

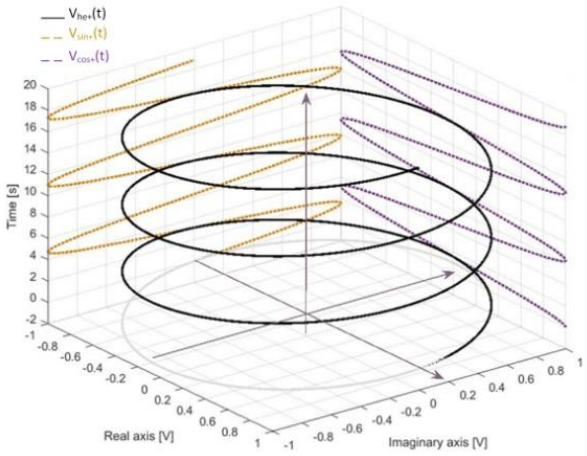


Fig. 3. Waveforms of $V_{he+}(t)$, $V_{sin+}(t)$, and $V_{cos+}(t)$ functions.

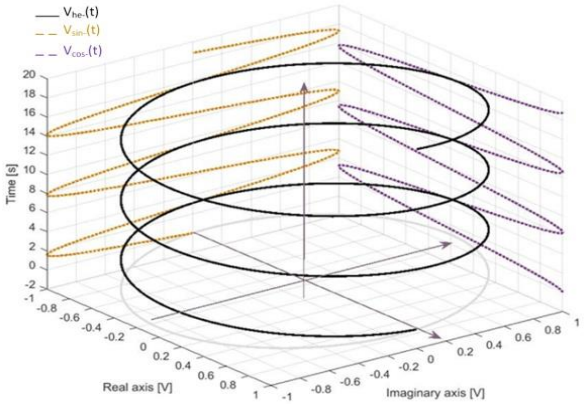


Fig. 4. Waveforms of $V_{he\text{-}}(t)$, $V_{sin\text{-}}(t)$, and $V_{cos\text{-}}(t)$ functions.

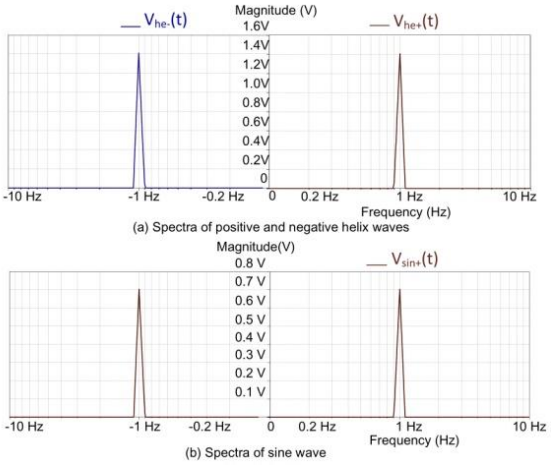


Fig. 5. Spectra of helix and sine waves.

B. *Characteristics of multi-harmonic signals*

In this section, the characteristics of multi-harmonic signals are analysed. It's well known that a square wave is a multi-harmonic signal. Fourier series expansion shows that any periodic signal can be written as a sum of harmonic signals having exactly integral number of cycles within the period time [26]. In other words, power series and Fourier's series are the simplified forms of the superposition principle

Copyright © AJSE Publishers

for the multi-harmonic signals. In time domain, a square signal $V_{sq}(t)= Asq(\omega_0 t+\Theta_0)$ can be defined in (12). Fig. 6 shows the waveform of a square signal and a ninth-order multi-harmonic sinusoidal wave. In laboratory simulation and practical measurement, the signal spectrum and system spectrum are usually investigated in the positive frequency domain or a half-side spectrum [27]. In addition, the concept of negative frequency for signal and system is still not well defined. Hence, the signal spectra of the common waves are written in the forms of half-side spectrum. Based on the superposition principle for analogue signals, the signal spectrum for the square wave is given in (13).

$$V_{sq}(t) = Asq\left(\omega_0 t+\theta_0\right) = A\left(\frac{1}{2}+\sum_{n=1}^{\infty}\frac{\sin\left[\left(2n+1\right)\omega_0 t+\theta_0\right]}{\left(2n+1\right)\pi}\right) \tag{12}$$

$$\left|V_{sq}(T_0)\right| = \left|Asq\left(\omega_0 T_0+\theta_0\right)\right| = A\left(\frac{1}{2}+\sum_{n=1}^{\infty}\frac{\sqrt{2}e^{j\left(\left(2n+1\right)\omega_0 T_0+\theta_0+\frac{\pi}{2}\right)}}{2\left(2n+1\right)\pi}\right) \tag{13}$$

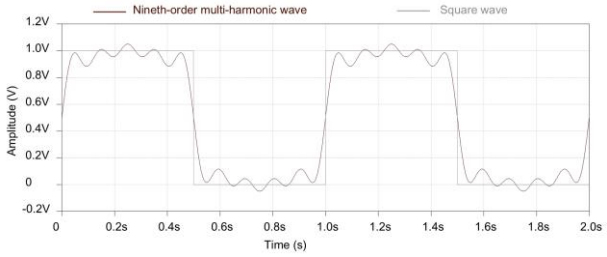


Fig. 6. Square wave and a ninth-order Fourier series.

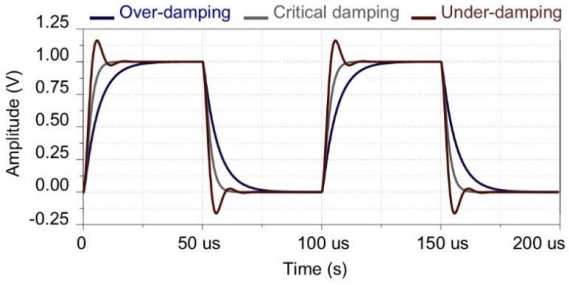


Fig. 7. Waveforms of output square signals.

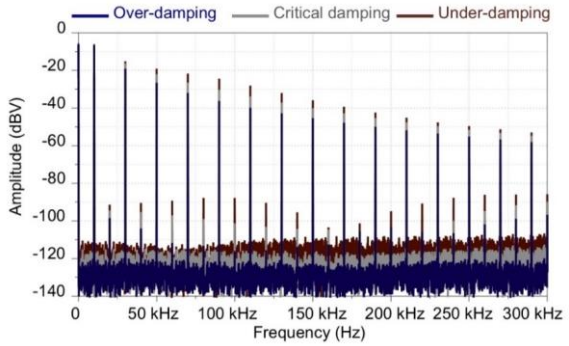


Fig. 8. Spectra of output square signals.

To do the ringing test for high-order systems, a square wave is usually used to put in the input port. Depending on the operating region of the system, the output waveforms can be over-damping, or critical damping, or under-damping as shown in Fig. 7. The spectra of the output square signals are plotted in Fig. 8. The ringing test will be analysed in detail in section V.

C. Characteristics of multi-phase signals

This section deals with the complex functions for the multi-phase signals in wireless communication systems. Multi-phase signals are used in wireless communication systems such as filters, amplifiers, frequency converters, and signal generators. The characteristics of the input sources are determined based on the transmission networks which are called single-ended systems, differential systems, complex systems, and polyphase systems [28]. So, single-ended signals such as sinusoidal signals and multi-harmonic signals are used in single-ended systems. The multi-phase signals can be divided into differential signals, complex signals, and polyphase signals. These signals are commonly used in fully differential amplifiers, polyphase filters, complex filters, and quadrature signal generation circuits. The normal sinusoidal signal on the real plane is the cosine wave. In the differential networks, there are two opposite-phase signal sources which are called differential signals. Let $V(t) = A\cos(\omega_0 t+\Theta_0)$ be a normal voltage, a differential signal $S_{dif}\{V_1,V_2\}$ can be defined as in (14). Hence, the half-side spectra in a referent plane of the differential signals are given in (15).

$$S_{dif}\left\{V_1;V_2\right\} = \left\{1;\left(\pm j\right)^2\right\}A\cos\left(\omega_0 t+\theta_0\right) \tag{14}$$

$$\left|S_{dif}\left\{V_1;V_2\right\}\right| = \left\{1;e^{\pm j\pi}\right\}\left|A\cos\left(\omega_0 T_0+\theta_0\right)\right| = \left\{1;e^{\pm j\pi}\right\}\frac{A\sqrt{2}}{2}e^{j(\omega_0 T_0+\theta_0)} \tag{15}$$

In the complex systems, there are two signal sources which are called complex signals. On the phase-order plane, the phase-orders of these signals are clockwise and anti-clockwise [29]. Let $V_p(t) = A\cos(\omega_0 t+\Theta_0)$ be a normal voltage, a positive complex signal $S_{cp}\{V_{p1},V_{p2}\}$ can be defined as in (16). Fig. 9 shows the waveforms of the positive complex signals on a real referent plane. The concepts of positive and negative angular frequencies are used to define the phase directions of complex signals in the frequency domain. The half-side spectra in a referent plane of the positive complex signals are given in (17). The anti-clockwise phase-order is a positive complex signal as shown in Fig. 10(c).

$$S_{cp}\left\{V_{p1};V_{p2}\right\} = \left\{1;\left(+j\right)\right\}A\cos\left(\omega_0 t+\theta_0\right) \tag{16}$$

$$\left|S_{cp}\left\{V_{p1};V_{p2}\right\}\right| = \left\{1;e^{+j\frac{\pi}{2}}\right\}\left|A\cos\left(\omega_0 T_0+\theta_0\right)\right| = \left\{1;e^{+j\frac{\pi}{2}}\right\}\frac{A\sqrt{2}}{2}e^{j(\omega_0 T_0+\theta_0)} \tag{17}$$

And, let $V_n(t) = A\cos(\omega_0 t+\Theta_0)$ be a normal voltage, a negative complex signal $S_{cn}\{V_{n1},V_{n2}\}$ can be defined as in (18). The half-side spectra in a referent plane of the negative complex signals are given in (19). The clockwise phase-order is a negative complex signal as shown in Fig. 10(d).

$$S_{cn}\{V_{n1};V_{n2}\} = \{1;(-j)\}A\cos(-\omega_0 t-\theta_0) \quad (18)$$

$$\begin{aligned}\left|S_{cn}\{V_{n1};V_{n2}\}\right| &= \left\{1;e^{-j\frac{\pi}{2}}\right\}\left|A\cos(-\omega_0 T_0-\theta_0)\right| \\ &= \left\{1;e^{-j\frac{\pi}{2}}\right\}\frac{A\sqrt{2}}{2}e^{j(-\omega_0 T_0-\theta_0)}\end{aligned} \quad (19)$$

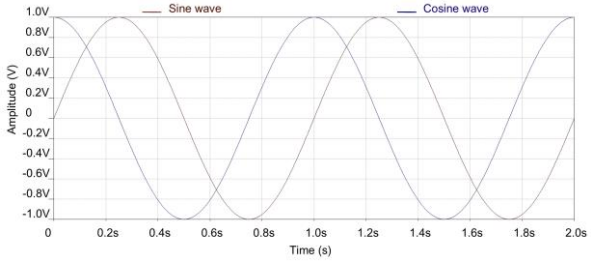


Fig. 9. Waveforms of sine and cosine functions in time domain.

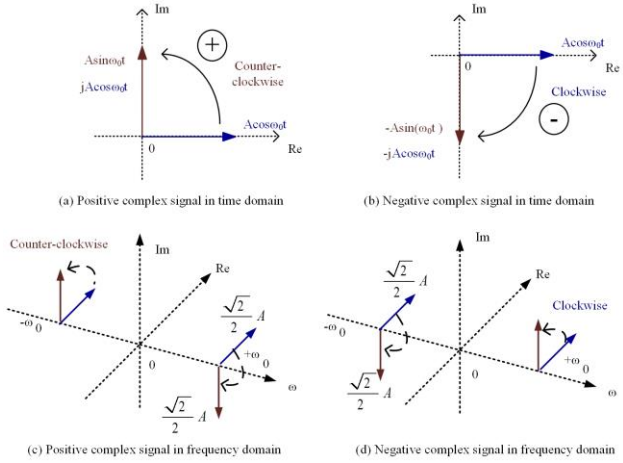


Fig. 10. Vectors of complex signals in time and frequency domains.

In polyphase networks, there are four signal sources which are called polyphase signals. In order words, polyphase signals are the differential forms of complex signals. Let $V_p(t) = A\cos(\omega_0 t+\Theta_0)$ be a normal voltage, a positive polyphase signal $S_p\{V_{p1},V_{p2},V_{p3},V_{p4}\}$ can be defined as in (20). The phase-order of polyphase signals is also used to define the polarity of the multi-phase signals. The half-side spectra in a referent plane of the positive polyphase signals are given in (21).

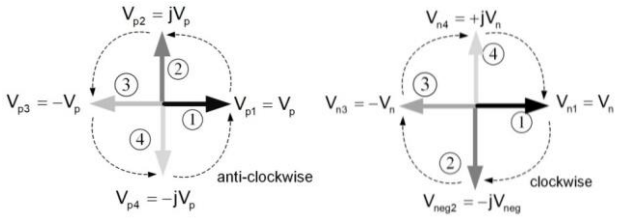
$$S_P\{V_{p1};V_{p2};V_{p3};V_{p4}\} = \{1;(+j);(+j)^2;(+j)^3\}A\cos(\omega_0 t+\theta_0) \quad (20)$$

$$\begin{aligned}\left|S_P\{V_{p1};V_{p2};V_{p3};V_{p4}\}\right| &= \left\{1;e^{+j\frac{\pi}{2}};e^{+j\pi};e^{+j\frac{3\pi}{2}}\right\}\left|A\cos(\omega_0 T_0+\theta_0)\right| \\ &= \left\{1;e^{+j\frac{\pi}{2}};e^{+j\pi};e^{+j\frac{3\pi}{2}}\right\}\frac{A\sqrt{2}}{2}e^{j(\omega_0 T_0+\theta_0)}\end{aligned} \quad (21)$$

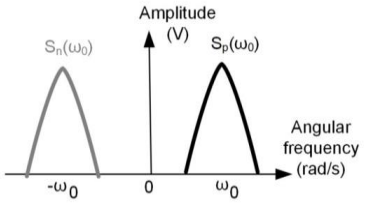
And, let $V_n(t) = A\cos(\omega_0 t+\Theta_0)$ be a normal voltage, a negative polyphase signal $S_n\{V_{n1},V_{n2},V_{n3},V_{n4}\}$ can be defined as in (22). The half-side spectra in a referent plane of the negative complex signals are given in (23). The clockwise phase-order is a negative polyphase signal and vice versa as shown in Fig. 11(a). The angular frequency variables ω and -ω are proposed to represent these signals on the angular frequency plane as described in Fig. 11(b).

$$S_n\{V_{n1};V_{n2};V_{n3};V_{n4}\} = \{1;(-j);(-j)^2;(-j)^3\}A\cos(-\omega_0 t-\theta_0) \quad (22)$$

$$\begin{aligned}\left|S_n\{V_{n1};V_{n2};V_{n3};V_{n4}\}\right| &= \left\{1;e^{-j\frac{\pi}{2}};e^{-j\pi};e^{-j\frac{3\pi}{2}}\right\}\left|A\cos(-\omega_0 T_0-\theta_0)\right| \\ &= \left\{1;e^{-j\frac{\pi}{2}};e^{-j\pi};e^{-j\frac{3\pi}{2}}\right\}\frac{A\sqrt{2}}{2}e^{j(-\omega_0 T_0-\theta_0)}\end{aligned} \quad (23)$$



(a) Phase-order of positive and negative polyphase signals.



(b) Polyphase signals on the angular frequency plane.

Fig. 11. Characteristics of positive and negative polyphase signals.

D. Summary of characteristics of common analogue signals

In this section, the characteristics of waveforms and spectra of some common single-ended, multi-harmonic, and multi-phase signals are summarized. TABLE I shows the properties of helix signals, sinusoidal signals, square waves, differential signals, complex signals, polyphase signals in both time and frequency domains.

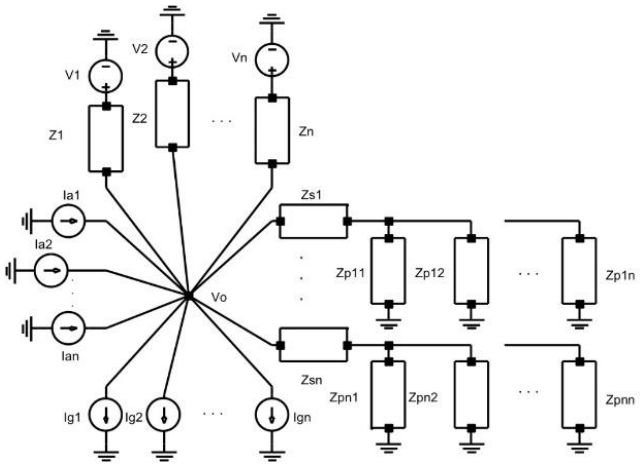


Fig. 12. Voltage at one node caused by multiple sources.

TABLE I. SIGNAL SPECTRUM OF COMMON ANALOG SIGNALS.

Signal type	Time domain	Half-side spectrum
Positive helix	$Ahe(\omega_0 t+\theta_0)$	$A\sqrt{2}e^{j(\omega_0 T_0+\theta_0)}$
Negative helix	$Ahe(-\omega_0 t-\theta_0)$	$A\sqrt{2}e^{j(-\omega_0 T_0-\theta_0)}$
Cosine	$A\cos(\omega_0 t+\theta_0)$	$\frac{A\sqrt{2}}{2}e^{j(\omega_0 T_0+\theta_0)}$
Sine	$A\sin(\omega_0 t+\theta_0)$	$\frac{A\sqrt{2}}{2}e^{j\left(\omega_0 T_0+\theta_0+\frac{\pi}{2}\right)}$
Square	$Asq(\omega_0 t+\theta_0)$ $=A\left(\frac{1}{2}+\sum_{n=1}^{\infty}\frac{\sin\left[(2n+1)\omega_0 t+\theta_0\right]}{(2n+1)\pi}\right)$	$\lvert Asq(\omega_0 T_0+\theta_0\rvert$ $=A\left(\frac{1}{2}+\sum_{n=1}^{\infty}\frac{\sqrt{2}e^{j\left((2n+1)\omega_0 T_0+\theta_0+\frac{\pi}{2}\right)}}{2(2n+1)\pi}\right)$
Differential cosine	$\left\{1;(\pm j)^2\right\}A\cos(\omega_0 t+\theta_0)$	$\left\{1;e^{\pm j\pi}\right\}\frac{A\sqrt{2}}{2}e^{j(\omega_0 T_0+\theta_0)}$
Differential sine	$\left\{1;(\pm j)^2\right\}A\sin(\omega_0 t+\theta_0)$	$\left\{1;e^{\pm j\pi}\right\}\frac{A\sqrt{2}}{2}e^{j\left(\omega_0 T_0+\theta_0+\frac{\pi}{2}\right)}$
Positive complex	$\{1;+j\}A\cos(\omega_0 t+\theta_0)$	$\left\{1;e^{+j\frac{\pi}{2}}\right\}\frac{A\sqrt{2}}{2}e^{j(\omega_0 T_0+\theta_0)}$
Negative complex	$\{1;-j\}A\cos(-\omega_0 t-\theta_0)$	$\left\{1;e^{-j\frac{\pi}{2}}\right\}\frac{A\sqrt{2}}{2}e^{j(-\omega_0 T_0-\theta_0)}$
Positive polyphase	$\left\{1;+j;(+j)^2;(+j)^3\right\}A\cos(\omega_0 t+\theta_0)$	$\left\{1;e^{+j\frac{\pi}{2}};e^{+j\pi};e^{+j\frac{3\pi}{2}}\right\}$ $\frac{A\sqrt{2}e^{j(\omega_0 T_0+\theta_0)}}{2}$
Negative polyphase	$\left\{1;-j;(-j)^2;(-j)^3\right\}A\cos(-\omega_0 t-\theta_0)$	$\left\{1;e^{-j\frac{\pi}{2}};e^{-j\pi};e^{-j\frac{3\pi}{2}}\right\}$ $\frac{A\sqrt{2}}{2}e^{j(-\omega_0 T_0-\theta_0)}$

IV. PROPOSAL OF SUPERPOSITION FORMULA

A. *Definition of superposition formula*

In this section, a superposition formula is proposed to derive the transfer function in multi-source networks. The main purpose of this formula is that the actuating voltage and current sources can be expressed separately with the node voltage, and the effects of these sources can be computed at one time. Let $V_o(t)$ be a general voltage at one node. Assume that current $I_i(t)$ and voltage $V_i(t)$ are the actuating current and voltage sources, the total currents caused by a node voltage $V_O(t)$ are equal to the sum of currents distributed by each actuating source. The direction of the current source is positive as its arrow goes ahead into a node, and negative as its arrow goes toward the ground as shown in Fig. 12. The ahead-arrow and ground-arrow current sources are denoted by $I_a(t)$ and $I_g(t)$. The voltage node equation for multiple currents and multiple voltages is expressed in (24). If the impedances are divided into small branches, voltage at one node will be calculated by the impedances of every branch [30]. Here, Z_{si} are sub-series impedances, and Z_{pii} are sub-parallel impedances. The simplified superposition theorem formula is a standard nodal analysis equation for all types of actuating sources (direct current/voltage sources, alternating current/voltage sources, dependent and independent current/voltage sources, multiphase current/voltage sources), and all types of loads (resistor, capacitor, inductor, transistor) [31].

$$V_O(t)\left(\sum_{i=1}^{n}\frac{1}{Z_i}+\sum_{i=1}^{n}\frac{1}{Z_{si}+\frac{1}{\sum_{k=1}^{n}\frac{1}{Z_{pik}}}}\right)=\sum_{i=1}^{n}\left(\frac{V_i(t)}{Z_i}+I_{ai}(t)-I_{gi}(t)\right) \quad (24)$$

B. *Behaviour of 4th-order RC polyphase filter*

In this section, the behaviors of a 4th-order polyphase filter shall be analyzed. Fig. 13 shows the schematic diagram of a 4th-order RC polyphase filter. As the input signal sources are the positive polyphase signals $S_p\{V_1; V_2; V_3; V_4\}=\{1;(+j);(+j)^2;(+j)^3\}V(t)$, after the proposed superposition theorem is applied at each node, the current node equations at nodes V_a, V_b, V_c, and V_{out} are derived in (25). The impedances in the sub-branches are calculated by the impedances of every branch [32].

$$\begin{aligned}
&V_{out}\left(\frac{1}{Z_{C1}}+\frac{1}{R_1}\right)=\frac{V_a}{R_1}+\frac{(+j)^3V_a}{Z_{C1}};V_a\left(\frac{1}{Z_{C2}}+\frac{1}{R_2}+\frac{2}{M_A}\right)=\frac{V_a}{R_2}+\frac{(+j)^3V_b}{Z_{C2}};\\
&V_b\left(\frac{1}{Z_{C3}}+\frac{1}{R_3}+\frac{1}{M_{B1}}+\frac{1}{M_{B2}}\right)=\frac{V_c}{R_3}+\frac{(+j)^3V_c}{Z_{C3}};\\
&V_c\left(\frac{1}{Z_{C4}}+\frac{1}{R_4}+\frac{1}{M_{C1}}+\frac{1}{M_{C2}}\right)=\frac{V_{in}}{R_4}+\frac{(+j)^3V_{in}}{Z_{C4}};\\
&M_A=R_1+Z_{C1};M_{B1}=R_2+\frac{1}{\frac{1}{Z_{C2}}+\frac{2}{M_A}};M_{B2}=Z_{C2}+\frac{1}{\frac{1}{R_2}+\frac{2}{M_A}};\\
&M_{C1}=R_3+\frac{1}{\frac{1}{Z_{C3}}+\frac{1}{M_{B1}}+\frac{1}{M_{B2}}};M_{C2}=Z_{C3}+\frac{1}{\frac{1}{R_3}+\frac{1}{M_{B1}}+\frac{1}{M_{B2}}};
\end{aligned} \quad (25)$$

Then, the transfer function of this polyphase filter in the positive frequency domain is given in (26).

$$H_P(\omega)=\frac{b_{0P}(j\omega)^4+b_{1P}(j\omega)^3+b_{2P}(j\omega)^2+b_{3P}j\omega+1}{a_0(j\omega)^4+a_1(j\omega)^3+a_2(j\omega)^2+a_3j\omega+1}; \quad (26)$$

As the input sources are negative polyphase signals $S_n\{V_1; V_2; V_3; V_4\} = \{1; (-j); (-j)^2; (-j)^3\}$ V(t), the transfer function of the 4th-order polyphase filter in the negative frequency domain is given in (27).

$$H_N(\omega)=\frac{b_{0N}(j\omega)^4+b_{1N}(j\omega)^3+b_{2N}(j\omega)^2+b_{3N}j\omega+1}{a_0(j\omega)^4+a_1(j\omega)^3+a_2(j\omega)^2+a_3j\omega+1}; \quad (27)$$

Hence, the image rejection ratio of this polyphase filter is derived in (28). The values of the constant variables of the 4th-order RC polyphase filter are given in TABLE II. The entire device parameters of the 4th-order RC polyphase filter are summarized in TABLE III. Fig. 14 shows the simulation result of the proposed design of 4th-order polyphase filter. The image signal rejection ratio of this model is 36 dB. It is properly considered for a narrow band low-IF receiver.

Copyright © AJSE Publishers

$$IRR(\omega)=\frac{b_{0P}(j\omega)^4+b_{1P}(j\omega)^3+b_{2P}(j\omega)^2+b_{3P}j\omega+1}{b_{0N}(j\omega)^4+b_{1N}(j\omega)^3+b_{2N}(j\omega)^2+b_{3N}j\omega+1}; \quad (28)$$

TABLE II. VALUES OF GIVEN VARIABLES OF RC POLYPHASE FILTER.

Variable	Value
$\mathbf{b_{0P}}$	$(+j)^{12}R_1R_2R_3R_4C_1C_2C_3C_4$
$\mathbf{b_{1P}}$	$(+j)^9\left[R_1R_2C_1C_2(R_3C_3+R_4C_4)+R_3R_4C_3C_4(R_1C_1+R_2C_2)\right]$
$\mathbf{b_{2P}}$	$(+j)^6\left[R_1C_1(R_2C_2+R_3C_3+R_4C_4)+R_2C_2(R_3C_3+R_4C_4)+R_3C_3R_4C_4\right]$
$\mathbf{b_{3P}}$	$(+j)^3(R_1C_1+R_2C_2+R_3C_3+R_4C_4)$
$\mathbf{b_{0N}}$	$(-j)^{12}R_1R_2R_3R_4C_1C_2C_3C_4$
$\mathbf{b_{1N}}$	$(-j)^9\left[R_1R_2C_1C_2(R_3C_3+R_4C_4)+R_3R_4C_3C_4(R_1C_1+R_2C_2)\right]$
$\mathbf{b_{2N}}$	$(-j)^6\left[R_1C_1(R_2C_2+R_3C_3+R_4C_4)+R_2C_2(R_3C_3+R_4C_4)+R_3C_3R_4C_4\right]$
$\mathbf{b_{3N}}$	$(-j)^3(R_1C_1+R_2C_2+R_3C_3+R_4C_4)$
$\mathbf{a_0}$	$R_1R_2R_3R_4C_1C_2C_3C_4$
$\mathbf{a_1}$	$R_1R_2R_3C_1C_2C_3+R_2R_3R_4(C_2C_3C_4+2C_1C_2C_3+2C_1C_2C_4+2C_1C_3C_4)$ $+R_1R_2R_4C_1C_2(2C_3+C_4)+R_1R_3R_4(C_1C_3C_4+2C_1C_2C_3+2C_1C_2C_4)$
$\mathbf{a_2}$	$R_1R_2C_1C_2+R_3R_4(C_3C_4+2C_1C_4+2C_1C_2+2C_1C_3+2C_2C_3)$ $R_1R_3(C_1C_3+2C_1C_2)+R_2R_4(C_2C_4+2C_1C_2+2C_1C_4+2C_2C_3+4C_1C_3)$ $R_1R_4(C_1C_4+2C_1C_2+2C_1C_3)+R_2R_3(C_2C_3+2C_1C_2+2C_1C_3)$
$\mathbf{a_3}$	$R_1C_1+R_2(2C_1+C_2)+R_3(2C_1+2C_2+C_3)+R_4(2C_1+2C_2+2C_3+C_4)$

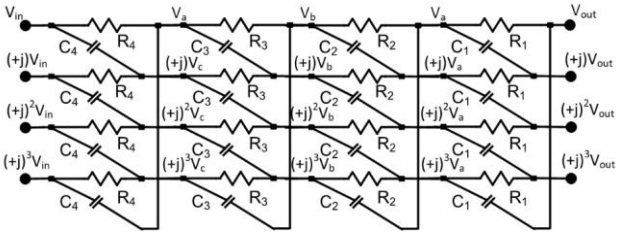


Fig. 13. Schematic of the 4th-order RC polyphase filter.

TABLE III. PARAMETERS OF RC POLYPHASE FILTER.

	Stage 1	Stage 2	Stage 3	Stage 4
Resistor	$\mathbf{R_1}$	$\mathbf{R_2}$	$\mathbf{R_3}$	$\mathbf{R_4}$
Value	**1 kΩ**	**1 kΩ**	**1 kΩ**	**1 kΩ**
Capacitor	$\mathbf{C_1}$	$\mathbf{C_2}$	$\mathbf{C_3}$	$\mathbf{C_4}$
Value	**227 pF**	**106 pF**	**39.8 pF**	**19.9 pF**
Cut-off frequency	$\mathbf{f_1}$	$\mathbf{f_2}$	$\mathbf{f_3}$	$\mathbf{f_4}$
Value	**0.7 MHz**	**1.5 MHz**	**4 MHz**	**8 MHz**

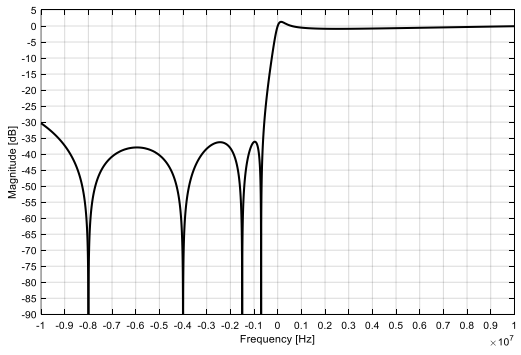


Fig. 14. Simulation result of the 4th-order RC polyphase filter.

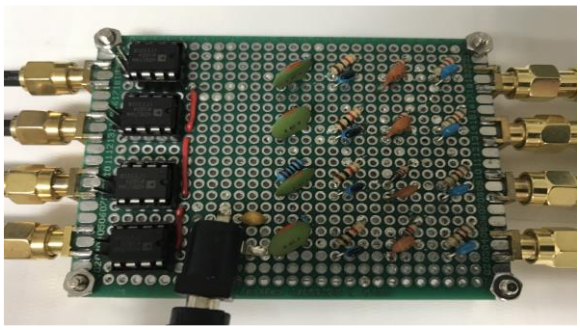


Fig. 15. Implemented circuit for the 4th-order RC polyphase filter.

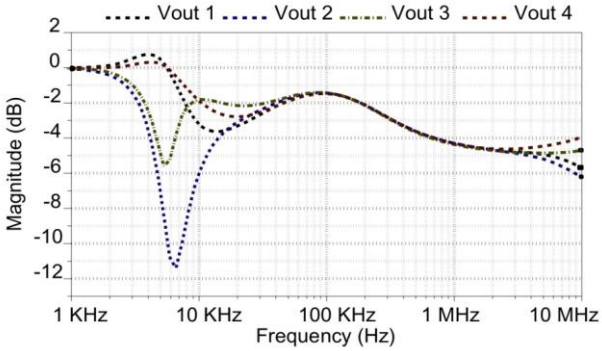


Fig. 16. Behaviors of pass-band gain of the 4th-order RC polyphase filter.

In practical design, the parasitic elements and the value variation of chosen components will affect the behavior of the circuit [33]. Fig. 16 shows the frequency responses of the pass-band gain of the implemented 4th-order RC polyphase filter. The IQ mismatches occurred at below 40 kHz and above 2 MHz in the range from 1 kHz to 10 MHz. The IQ mismatches were caused by the parasitic elements and the value variation of the R, C components. In addition, the limitations of the measurement equipment and the characteristics of the active unity-gain circuits also affected the measurement results [34].

C. Merits of proposed superposition formula

In this section, the merits of the proposed superposition formula are presented. There are some new concepts of multi-source signals such as negative and positive frequency, negative and positive complex signals, negative and positive polyphase signals, and spectrum of multi-source signals which are not well defined in the conventional methods [35]. In addition, there is not a general formula for analyzing the behaviors of multi-source networks. In a circuit having more than one independent source, the effects of all the sources can be considered at one time [36]. From the concept of the proposed formula, the transfer function of a multi-source network can be easily derived. The superposition formula was used to compare with the conventional superposition principle and the Millan's theorem as shown in TABLE IV. However, Millan's theorem is not widely applied in multi-source network analysis. Furthermore, the behaviours of feedback amplifiers with Miller capacitance due to parasitic capacitance between the output and input of active devices are simply analysed based on the proposed formula [37].

Copyright © AJSE Publishers

TABLE IV. COMPARISON OF PROPOSED METHOD WITH OTHER METHODS.

Features	Superposition formula	Conventional Superposition	Millan's theorem
Effects of all actuating sources	**one time**	**Several times**	**one time**
Transfer function accuracy	**Yes**	**No**	**No**
Single-input network analysis	**Yes**	**Yes**	**Yes**
Polyphase network analysis	**Yes**	**No**	**No**
Complex network analysis	**Yes**	**No**	**No**
Image rejection ratio accuracy	**Yes**	**No**	**No**

V. BEHAVIOURS OF RAUCH LOW-PASS FILTERS

A. *Operating regions of high-order systems*

In this section, the operating regions of high-order systems shall be reviewed. Ringing represents the voltage overshoot or current overshoot. It can be seen in many research papers, in datasheets of the commercial operational amplifiers, in the negative feedback amplifiers, and in the feedback control systems. Complex functions for transmission networks are usually expressed in three forms: magnitude-angular plots (Bode plots), polar charts (Nyquist charts), and magnitude-argument diagrams (Nichols diagrams) [38]. When the input source, output signal, and some other sources in the internal dynamics of a network are known, the transfer function is used to examine the behavior of the network. The transfer function H(ω) of a filter is the ratio of the output signal $V_{out}(\omega)$ to the input signal $V_{in}(\omega)$ as a function of the frequency. A simplified transfer function is rewritten as in (29). The term "self-loop function" is proposed to define L(ω) for linear networks in both cases with and without feedback systems.

$$H(\omega)=\frac{V_{out}(\omega)}{V_{in}(\omega)}=\frac{A(\omega)}{1+L(\omega)} \tag{29}$$

where, A(ω) is the numerator function of the transfer function. Fig. The phase margin of the self-loop function is directly related to the transient response of a system. It shows how much the phase margin can be increased before the system becomes unstable.

In a 2nd-order system, the operating regions are over-damping, critical damping, and under-damping. In the over-damping region, the amplitudes of high-order harmonics of the step signal are significantly reduced from the first cut-off angular frequency; therefore, the rising time is short [39]. The transfer function and the self-loop function of a 2nd-order system are given in (30). The properties of a second-order system are summarized in TABLE V. Three typical cases of a second-order system are given to determine the operating region of the circuit as shown in Eq. (31). The coefficients of the transfer functions are

- Under-damped (binomial coefficients ratio is 1:1:1),
- Critically damped (binomial coefficients ratio is 1:2:1),
- Over-damped (binomial coefficients ratio is 1:3:1).

$$H(\omega)=\frac{b_0}{a_0(j\omega)^2+a_1 j\omega+1};\ L(\omega)=a_0(j\omega)^2+a_1 j\omega; \tag{30}$$

TABLE V. OPERATING REGIONS OF 2ND-ORDER SELF-LOOP FUNCTION

Case	Over-damping	
Delta (Δ)	$\Delta=a_1^2-4a_0>0$	
$\lvert L(\omega)\rvert$	$\omega\sqrt{(a_0\omega)^2+a_1^2}$	
θ(ω)	$\frac{\pi}{2}+\arctan\frac{a_0\omega}{a_1}$	
$\omega_1=\frac{b}{2a}\sqrt{\sqrt{5}-2}$	$\lvert L(\omega_1)\rvert>1$	$\pi-\theta(\omega_1)>76.3^o$
Case	Critical damping	
Delta (Δ)	$\Delta=a_1^2-4a_0=0$	
$\lvert L(\omega)\rvert$	$\omega\sqrt{(a_0\omega)^2+a_1^2}$	
θ(ω)	$\frac{\pi}{2}+\arctan\frac{a_0\omega}{a_1}$	
$\omega_1=\frac{b}{2a}\sqrt{\sqrt{5}-2}$	$\lvert L(\omega_1)\rvert=1$	$\pi-\theta(\omega_1)=76.3^o$
Case	Under-damping	
Delta (Δ)	$\Delta=a_1^2-4a_0<0$	
$\lvert L(\omega)\rvert$	$\omega\sqrt{(a_0\omega)^2+a_1^2}$	
θ(ω)	$\frac{\pi}{2}+\arctan\frac{a_0\omega}{a_1}$	
$\omega_1=\frac{b}{2a}\sqrt{\sqrt{5}-2}$	$\lvert L(\omega_1)\rvert<1$	$\pi-\theta(\omega_1)<76.3^o$

$$\begin{aligned}
H_1(\omega)&=\frac{1}{(j\omega)^2+j\omega+1};\ L_1(\omega)=(j\omega)^2+j\omega;\\
H_2(\omega)&=\frac{1}{(j\omega)^2+2j\omega+1};\ L_2(\omega)=(j\omega)^2+2j\omega;\\
H_3(\omega)&=\frac{1}{(j\omega)^2+3j\omega+1};\ L_3(\omega)=(j\omega)^2+3j\omega;
\end{aligned} \tag{31}$$

The Bode plot of these transfer functions, the Nichols plot of these self-loop functions, transient responses are shown in Fig. 17, Fig. 18, and Fig. 19, respectively. The phase margin is observed at unity gain of the self-loop function. The simulation results of the self-loop functions show that

- In the over-damping region, the phase margin is 82 degrees (observed at 98 degrees),
- In the critical damping region, the phase margin is 76.3 degrees (observed at 103.7 degrees), and
- In the under-damping region, the phase margin is 35 degrees (observed at 145 degrees).

Copyright © AJSE Publishers

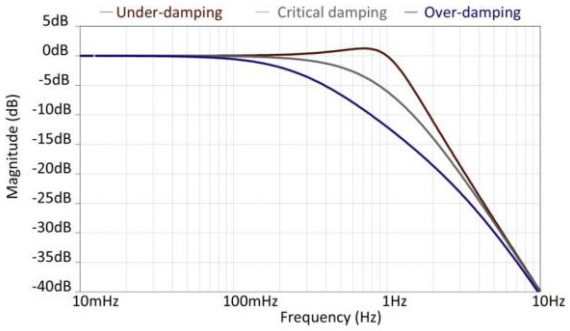


Fig. 17. Bode plot of the 2nd-order transfer function.

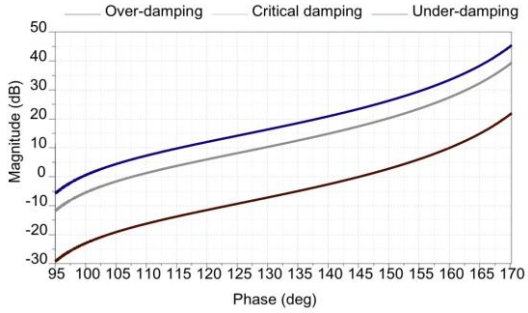


Fig. 18. Nichols chart of the 2nd-order self-loop function.

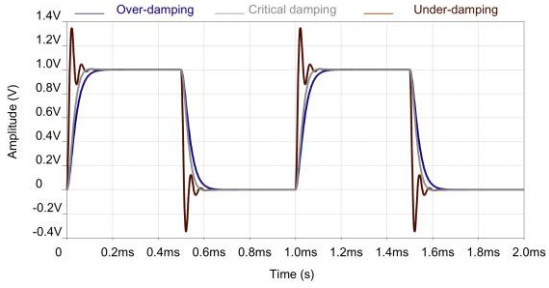


Fig. 19. Transient responses of the 2nd-order self-loop function.

The use of Pascal's triangle is a simple way to calculate the binomial coefficients of a high-order polynomial. In addition, the properties of the binomial coefficients can be also used to determine the operating regions of high-order systems [40]. In general, the coefficients of the expanded polynomial $(j\omega+1)^n$ are defined as shown in Eq. (32). For instance, based on the 4th row of Pascal's triangle as shown in Table VI, the binomial coefficients of the expanded polynomial are simplified as 1 : 4 : 6 : 4 : 1.

$$(j\omega+1)^n = a_0(j\omega)^n + a_1(j\omega)^{n-1} + \ldots + a_{n-1}j\omega + 1 \quad (32)$$

TABLE VI. PASCAL'S TABLE OF THE BINOMIAL COEFFICIENTS

	Binomial coefficients						
Row2			**1**	**2**	**1**		
Row3		**1**	**3**	**3**	**1**		
Row4	**1**	**4**	**6**	**4**	**1**		
Row5	**1**	**5**	**10**	**10**	**5**	**1**	
Row6	**1**	**6**	**15**	**20**	**15**	**6**	**1**

B. *Behaviours of op amp without frequency compensation*

In this section, the behaviors of a single-ended two-stage CMOS operational amplifier (op amp) without frequency compensation will be presented. Operational amplifiers are used in many applications such as unity-gain amplifiers, inverting amplifiers, and active analog filters [41]. The overall performance of these circuits may be stable or not. Thus, the stability test and the frequency compensation of this op amp are of interest [42]. Fig. 20 shows the schematic of a single-ended two-stage op amp without frequency compensation. A half small signal model of this op amp is drawn in Fig. 21. In the conventional Miller approximation, the interpretation of the Miller capacitance is very difficult because there are two loading capacitors in this two-stage op amp. After applying the proposed superposition theorem at each node, the current node equations at nodes V_a, V_b, and V_{out} are derived in (33).

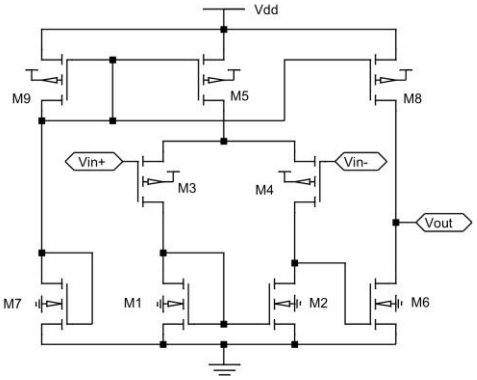


Fig. 20. Schematic of an op amp without frequency compensation

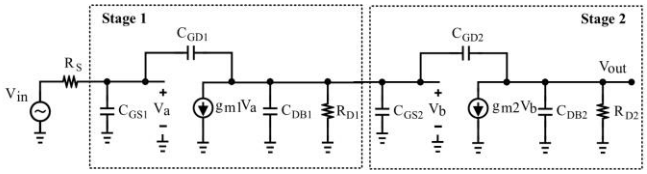


Fig. 21. Small signal model of the op amp without frequency compensation.

$$\begin{aligned}
&V_a\left[\frac{1}{R_S}+j\omega(C_{GS1}+C_{GD1})\right]=\frac{V_{in}}{R_S}+V_b j\omega C_{GD1};\\
&V_b\left[j\omega(C_{GD1}+C_{DB1}+C_{GS2}+C_{GD2})+\frac{1}{R_{D1}}\right]=V_a(j\omega C_{GD1}-g_{m1})+V_{out}j\omega C_{GD2};\\
&V_{out}\left[j\omega(C_{GD2}+C_{DB2})+\frac{1}{R_{D2}}\right]=V_b(j\omega C_{GD2}-g_{m2});
\end{aligned} \quad (33)$$

Hence, the open-loop function A(ω) and the self-loop function L(ω) of this op amp are 3th-order complex functions as in (34). The values of the constant variables are given in TABLE VII. The gain-bandwidth (GBW) of this op amp is defined by the multiplication of the direct current gain A_0 and the cut-off frequency f_{BW}. The gain-bandwidth is also measured at unity gain ($GBW=A_0f_{BW}$). As the two-stage op amp is used to design a unity-gain amplifier as shown in Fig. 22, the overall performance of the circuit may be stable or not.

$$\begin{aligned}
&A(\omega)=\frac{V_{out}(\omega)}{V_{in}(\omega)}=\frac{b_0(j\omega)^2+b_1j\omega+b_2}{a_0(j\omega)^3+a_1(j\omega)^2+a_2j\omega+1};\\
&L(\omega)=a_0(j\omega)^3+a_1(j\omega)^2+a_2j\omega;
\end{aligned} \quad (34)$$

TABLE VII. VALUES OF GIVEN VARIABLES OF WITHOUT FREQUENCY COMPENSATION.

Variable	Value
$\mathbf{b_0}$	$R_{D1}R_{D2}C_{GD1}C_{GD2}$
$\mathbf{b_1}$	$-R_{D1}R_{D2}\left(C_{GD1}g_{m2}+C_{GD2}g_{m1}\right)$
$\mathbf{b_2}$	$R_{D1}R_{D2}g_{m1}g_{m2}$
$\mathbf{a_0}$	$R_S R_{D1}R_{D2}\left(C_{GS1}+C_{GD1}\right)\left[C_{DB2}C_{GD2}+\left(C_{DB2}+C_{GD2}\right)\left(C_{DB1}+C_{GS2}\right)\right]$ $+R_S R_{D1}R_{D2}C_{GS1}C_{GD1}\left(C_{DB2}+C_{GD2}\right)$
$\mathbf{a_1}$	$R_{D1}R_{D2}\left[C_{GD2}C_{DB2}+\left(C_{GD2}+C_{DB2}\right)\left(C_{GD1}+C_{DB1}+C_{GS2}\right)\right]$ $+R_{D1}R_{D2}R_S\left[g_{m1}C_{GD1}\left(C_{GD2}+C_{DB2}\right)+g_{m2}C_{GD2}\left(C_{GS1}+C_{GD1}\right)\right]$ $+R_{D1}R_S\left[C_{GS1}C_{GD1}+\left(C_{GS1}+C_{GD1}\right)\left(C_{DB1}+C_{GS2}+C_{GD2}\right)\right]$ $+R_{D2}R_S\left(C_{GS1}+C_{GD1}\right)\left(C_{DB2}+C_{GD2}\right)$
$\mathbf{a_2}$	$R_{D1}\left(C_{GD1}+C_{DB1}+C_{GS2}+C_{GD2}\right)+R_{D2}\left[C_{DB2}+C_{GD2}\left(1+R_{D1}g_{m2}\right)\right]$ $+R_S\left[C_{GS1}+C_{GD1}\left(1+g_{m1}R_{D1}\right)\right]$

After applying the superposition principle at node V_{out}, the output voltage is given in (35).

$$V_{out}=A(\omega)\left(V_{in}-V_{out}\right); \tag{35}$$

Hence, the transfer function H(ω) and the self-loop function L(ω) of the unity gain amplifier are derived in (36). The entire device parameters of the two-stage CMOS op amp are summarized in TABLE V. In this simulation, the transistor models of TSMC 0.18 um CMOS technology are used to perform the ringing test for this amplifier. The supply voltage is 1.8 V, and the bias circuit is not shown.

$$H(\omega)=\frac{V_{out}}{V_{in}}=\frac{1}{1+\dfrac{1}{A(\omega)}}\approx 1;\ L(\omega)=\frac{1}{A(\omega)}; \tag{36}$$

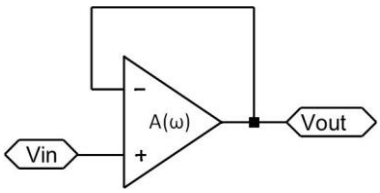


Fig. 22. Simplified model of the unity-gain amplifier circuit

TABLE VIII. PARAMETERS OF SINGLE-ENDED OP AMP.

Elements	Value (W/L)	Elements	Value (W/L)
M1	10 um / 300 nm	M5	10 um / 500 nm
M2	18 um / 300 nm	M6	1.7 um / 300 nm
M3	1.6 um / 800 nm	M7	4 um / 300 nm
M4	1.6 um / 800 nm	M8, M9	1 um / 300 nm

Fig. 23 and Fig. 24 show the Bode plot of the transfer function and the Nichols plot of the self-loop function of the unity-gain amplifier. The magnitude of the transfer function is very large (15 dB) at high frequency (2 GHz), and the phase margin at the unity gain of the self-loop function is very small (13 degrees). Therefore, overshoot and undershoot occur as shown in Fig. 25.

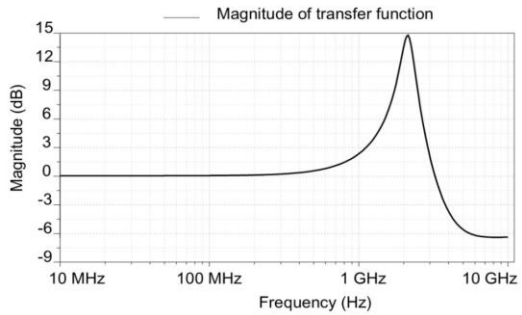


Fig. 23. Bode plot of the transfer function of the unity-gain amplifier.

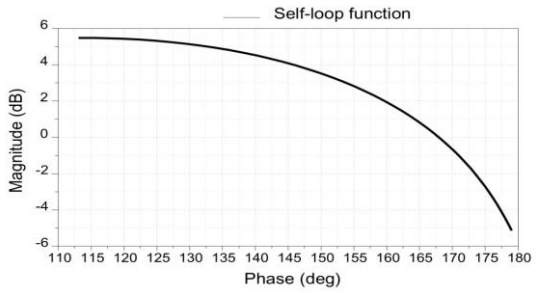


Fig. 24. Nichols plot of the self-loop function of the unity-gain amplifier.

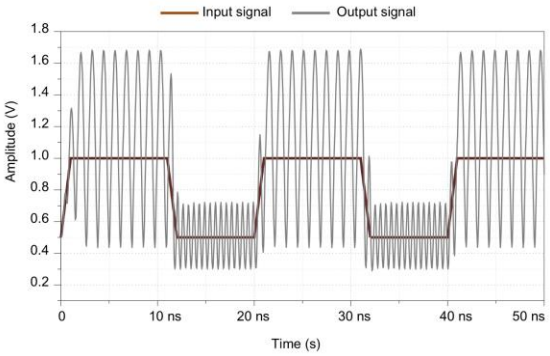


Fig. 25. Transient responses of the unity-gain amplifier.

C. Behaviours of a fully differential operational amplifier

In this section, the behaviors of a fully differential two-stage CMOS op amp with frequency compensation will be presented. Fig. 26 shows the schematic of a fully differential two-stage op amp with frequency compensation. A half small signal model of the fully differential two-stage op amp is drawn in Fig. 27. After applying the proposed superposition theorem at each node, the current node equations at nodes V_a, V_b, and V_{out} are derived in (37).

$$\begin{aligned}
&V_a\left[\frac{1}{R_S}+j\omega\left(C_{GS1}+C_{GD1}\right)\right]=\frac{V_{in}}{R_S}+V_b j\omega C_{GD1};\\
&V_b\left[j\omega\left(C_{GD1}+C_{DB1}+C_{GS2}+C_{GD2}\right)+\frac{1}{R_{D1}}+\frac{j\omega C_C}{1+j\omega R_C C_C}\right]\\
&\qquad=V_a\left(j\omega C_{GD1}-g_{m1}\right)+V_{out}\left(j\omega C_{GD2}+\frac{j\omega C_C}{1+j\omega R_C C_C}\right);\\
&V_{out}\left[j\omega\left(C_{GD2}+C_{DB2}\right)+\frac{j\omega C_C}{1+j\omega R_C C_C}+\frac{1}{R_{D2}}\right]=V_b\left(j\omega C_{GD2}+\frac{j\omega C_C}{1+j\omega R_C C_C}-g_{m2}\right);
\end{aligned} \tag{37}$$

Then, the open-loop function A(ω) and the self-loop function L(ω) of the fully differential two-stage op amp are 5th-order complex functions as in (38). The values of the constant variables are given in TABLE IX.

$$A(\omega)=\frac{V_{out}(\omega)}{V_{in}(\omega)}=\frac{b_0(j\omega)^4+b_1(j\omega)^3+b_2(j\omega)^2+b_3j\omega+b_4}{a_0(j\omega)^5+a_1(j\omega)^4+a_2(j\omega)^3+a_3(j\omega)^2+a_4j\omega+1}; \quad (38)$$
$$L(\omega)=a_0(j\omega)^5+a_1(j\omega)^4+a_2(j\omega)^3+a_3(j\omega)^2+a_4j\omega;$$

TABLE IX. VALUES OF GIVEN VARIABLES OF TWO-STAGE OP AMP WITH FREQUENCY COMPENSATION.

Variable	Value
$\mathbf{b_0}$	$R_{D1}R_{D2}R_C^2C_{GD1}C_{GD2}C_C^2$
$\mathbf{b_1}$	$R_CR_{D1}R_{D2}C_C\left[2C_{GD1}C_{GD2}+C_CC_{GD1}-R_CC_C\left(C_{GD1}g_{m2}+C_{GD2}g_{m1}\right)\right]$
$\mathbf{b_2}$	$R_{D1}R_{D2}C_{GD1}\left(C_{GD2}+C_C\right)$ $+R_{D1}R_{D2}R_CC_C\left(R_CC_Cg_{m1}g_{m2}-g_{m1}C_C-2g_{m1}C_{GD2}-2g_{m2}C_{GD1}\right)$
$\mathbf{b_3}$	$R_{D1}R_{D2}\left[2g_{m1}g_{m2}R_CC_C-g_{m1}\left(C_{GD2}+C_C\right)-g_{m2}C_{GD1}\right]$
$\mathbf{b_4}$	$R_{D1}R_{D2}g_{m1}g_{m2}$
$\mathbf{a_0}$	$R_SR_{D1}R_{D2}R_C^2C_C^2\left[C_{DB2}C_{GD2}\left(C_{GS1}+C_{GD1}\right)+C_{GS1}C_{GD1}\left(C_{DB2}+C_{GD2}\right)\right]$ $+R_SR_{D1}R_{D2}R_C^2C_C^2\left(C_{DB2}+C_{GD2}\right)\left(C_{GS1}+C_{GD1}\right)\left(C_{DB1}+C_{GS2}\right)$
$\mathbf{a_1}$	$R_{D1}R_{D2}R_C^2C_C^2\left[C_{GD2}C_{DB2}+\left(C_{GD2}+C_{DB2}\right)\left(C_{GD1}+C_{DB1}+C_{GS2}\right)\right]$ $+R_{D1}R_{D2}R_SR_C^2C_C^2\left[g_{m1}C_{GD1}\left(C_{GD2}+C_{DB2}\right)+g_{m2}C_{GD2}\left(C_{GS1}+C_{GD1}\right)\right]$ $+R_{D1}R_SR_C^2C_C^2\left[C_{GS1}C_{GD1}+\left(C_{GS1}+C_{GD1}\right)\left(C_{DB1}+C_{GS2}+C_{GD2}\right)\right]$ $+R_{D2}R_SR_C^2C_C^2\left(C_{GS1}+C_{GD1}\right)\left(C_{DB2}+C_{GD2}\right)$ $+R_{D1}R_{D2}R_SR_CC_C\left[2C_{DB2}C_{GD2}\left(C_{GS1}+C_{GD1}\right)+2C_{GS1}C_{GD1}\left(C_{GD2}+C_{DB2}\right)\right]$ $+R_{D1}R_{D2}R_SR_CC_C\left(C_{GS1}+C_{GD1}\right)\left(C_{GD2}+C_{DB2}\right)\left[2\left(C_{DB1}+C_{GS2}\right)+C_{GD2}\right]$ $+R_{D1}R_{D2}R_SR_CC_C^2\left[C_{DB2}\left(C_{GS1}+C_{GD1}\right)+C_{GS1}C_{GD1}+\left(C_{GS1}+C_{GD1}\right)\left(C_{DB1}+C_{GS2}\right)\right]$
$\mathbf{a_2}$	$2R_{D1}R_SR_CC_C\left[C_{GS1}C_{GD1}+\left(C_{GS1}+C_{GD1}\right)\left(C_{DB1}+C_{GS2}+C_{GD2}\right)\right]$ $+R_{D1}R_SR_CC_C\left[C_C\left(C_{GS1}+C_{GD1}\right)+R_{D2}g_{m2}C_{GD2}\left(C_{GS1}+C_{GD1}\right)\right]$ $+R_{D2}R_SR_CC_C\left(2C_{GD2}+2C_{DB2}+C_C\right)\left[C_{GS1}+C_{GD1}\left(1+g_{m1}R_{D1}\right)\right]$ $+2R_{D1}R_{D2}R_CC_C\left[C_{DB2}C_{GD2}+\left(C_{DB2}+C_{GD2}\right)\left(C_{GD1}+C_{DB1}+C_{GS2}\right)\right]$ $+R_{D1}R_{D2}R_CC_C^2\left(C_{GD1}+C_{DB1}+C_{GS2}+C_{DB2}+C_{GD2}g_{m2}R_C\right)$ $+R_{D1}R_{D2}R_SC_{GS1}C_{GD1}\left(C_{GD2}+C_{DB2}+C_C\right)$ $+R_{D1}R_{D2}R_SC_{DB2}\left(C_{GS1}+C_{GD1}\right)\left(C_{DB1}+C_{GS2}+C_{GD2}+C_C\right)$ $+R_{D1}R_{D2}R_S\left(C_{GS1}+C_{GD1}\right)\left(C_{DB1}+C_{GS2}+g_{m2}R_CC_C\right)\left(C_{GD2}+C_C\right)$ $+R_C^2C_C^2\left[R_{D1}\left(C_{GD1}+C_{DB1}+C_{GS2}+C_{GD2}\right)+R_{D2}\left(C_{GD2}+C_{DB2}\right)\right]$ $+R_SR_C^2C_C^2\left[C_{GS1}+C_{GD1}\left(1+g_{m1}R_{D1}\right)\right]$
$\mathbf{a_3}$	$2R_CC_C\left[R_{D1}\left(C_{GD1}+C_{DB1}+C_{GS2}+C_{GD2}\right)+R_S\left(C_{GS1}+C_{GD1}\right)\right]$ $+R_CC_C\left[C_C\left(R_C+R_{D1}+R_{D2}\right)+2R_{D2}\left(C_{GD2}+C_{DB2}\right)\right]$ $+R_{D1}R_S\left[C_{GS1}C_{GD1}+\left(C_{GS1}+C_{GD1}\right)\left(C_{DB1}+C_{GS2}+C_{GD2}+C_C\right)\right]$ $+R_{D2}R_S\left(C_{GS1}+C_{GD1}\right)\left(C_{GD2}+C_{DB2}+C_C\right)$ $+R_{D1}R_{D2}\left[C_{DB2}\left(C_{GD2}+C_C\right)+\left(C_{GD1}+C_{DB1}+C_{GS2}\right)\left(C_{GD2}+C_{DB2}+C_C\right)\right]$ $+R_{D1}R_Sg_{m1}C_{GD1}\left[2R_CC_C+R_{D2}\left(C_{GD2}+C_{DB2}+C_C\right)\right]$ $+R_{D1}R_{D2}g_{m2}\left[R_S\left(C_{GD2}+C_C\right)\left(C_{GS1}+C_{GD1}\right)+R_CC_C\left(2C_{GD2}+C_C\right)\right]$
$\mathbf{a_4}$	$R_{D1}\left(C_{GD1}+C_{DB1}+C_{GS2}+C_{GD2}+C_C\right)+R_{D2}\left(C_{GD2}+C_{DB2}+C_C\right)$ $+2R_CC_C+R_{D1}R_{D2gm2}\left(C_{GD2}+C_C\right)+R_S\left(C_{GS1}+C_{GD1}+R_{D1}g_{m1}C_{GD1}\right)$

In this simulation, the transistor models of TSMC 0.18 um CMOS technology are also used to design the fully differential op amp. The entire device parameters of this op amp are summarized in TABLE X. Fig. 28 shows the Bode plot of the open-loop function and the Nichols plot of the self-loop function in the proposed design of the two-stage op amp. The magnitude of the open-loop function is 55 dB at around cutoff frequency 1 MHz, and the phase margin at the unity gain of the self-loop function is 90 degrees.

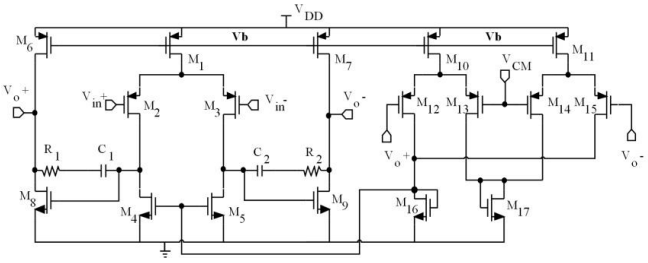


Fig. 26. Schematic of a fully differential two-stage op amp.

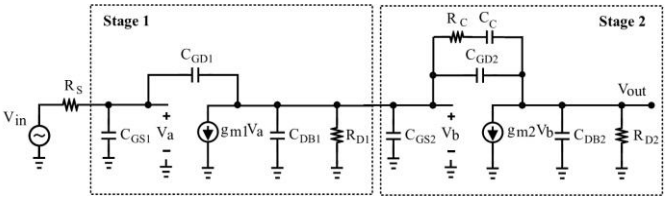


Fig. 27. Small signal model of the op amp with frequency compensation.

TABLE X. PARAMETERS OF OP AMP WITH FREQUENCY COMPENSATION.

Elements	Value	Elements	Value
M1	10 um / 300 nm	M11, M12	4 um / 300 nm
M2, M3	10 um / 180 nm	M13, M14	4 um / 300 nm
M4, M5	2 um / 300 nm	M15, M16	4 um / 300 nm
M6, M7	2 um / 180 nm	M17	4 um / 300 nm
M8, M9	10 um / 180 nm	M18	4 um / 300 nm
R1, R2	500 Ω	Vdd	1.8 V
C1, C2	500 fF	Vcm	0.9 V

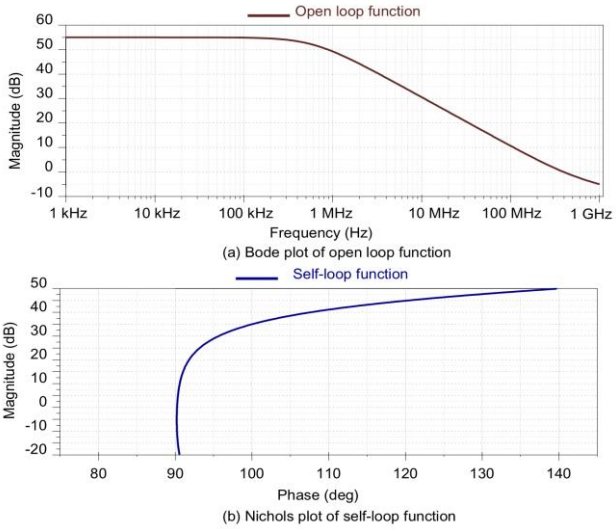


Fig. 28. Simulation results of the two-stage op amp.

D. Ringing test for a second-order Rauch LPF

In this section, the operating regions of a 2nd-order Rauch low-pass filter shall be analyzed. The single-ended form of this filter is shown in Fig. 29. After applying the proposed superposition theorem at each node, the current node equations at nodes V_A, V_B, and V_C are derived in (39).

$$V_A\left(\frac{1}{R_1}+\frac{1}{R_2}+j\omega C_1+\frac{1}{R_3}\right)=\frac{V_{in}}{R_1}+\frac{V_B}{R_2}+\frac{V_{out}}{R_3};$$
$$V_B\left(\frac{1}{R_2}+j\omega C_2\right)=\frac{V_A}{R_2}+V_{out}\,j\omega C_2; V_{out}=-V_B A(\omega); \quad (39)$$

Then, the transfer function and the self-loop function of the low-pass filter are given in (40).

$$H(\omega)=-\frac{b_0}{a_0(j\omega)^2+a_1 j\omega+1}; L(\omega)=a_0(j\omega)^2+a_1 j\omega;$$
$$b_0=\frac{R_3}{R_1};\ a_0=R_2R_3C_1C_2; a_1=\left(R_2+R_3+\frac{R_2R_3}{R_1}\right)C_2; \quad (40)$$

The operating regions of the Rauch low-pass filter can be determined through the passive components as in (41).

$$\frac{1}{R_2R_3C_1C_2}<\left(\frac{R_1R_2+R_1R_3+R_2R_3}{2R_1R_2R_3C_1}\right)^2; Over-damping$$
$$\frac{1}{R_2R_3C_1C_2}=\left(\frac{R_1R_2+R_1R_3+R_2R_3}{2R_1R_2R_3C_1}\right)^2; Critical\ damping \quad (41)$$
$$\frac{1}{R_2R_3C_1C_2}>\left(\frac{R_1R_2+R_1R_3+R_2R_3}{2R_1R_2R_3C_1}\right)^2; Under-damping$$

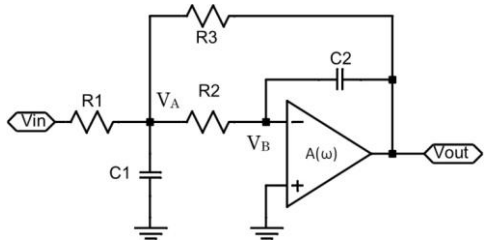


Fig. 29. Schematic diagram of a single-ended 2nd-order Rauch LPF.

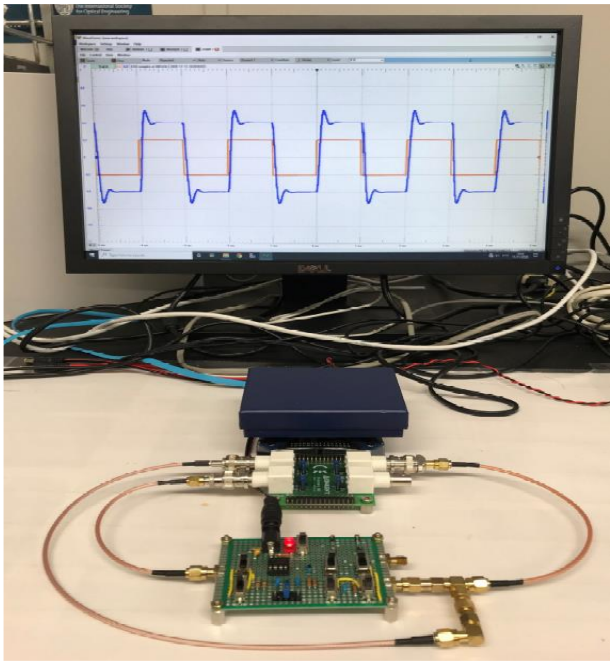


Fig. 30. Implemented circuit for the single-ended 2nd-order Rauch LPF.

A commercial op amp LM358 was used in this implementation. Fig. 30 shows the measurement set up of the implemented 2nd-order Rauch low-pass filter. The Bode plot of the transfer function, the Nichols plot of the self-loop function, and the transient response of the implemented circuit are shown in Figs. 31, 32, and 33, respectively. The measurement results of the self-loop functions in the implemented circuit show that

- In the over-damping region, the phase margin is 87 degrees (observed at 93 degrees),
- In the critical damping region, the phase margin is 80 degrees (observed at 100 degrees), and
- In the under-damping region, the phase margin is 50 degrees (observed at 130 degrees); therefore, the ringing occurs in the transient response of the under-damping region.

To reduce the white noise and random noise, the differential forms are used in many designs of high-order amplifiers and filters. Therefore, the differential forms of high-order systems have been studied recently [43].

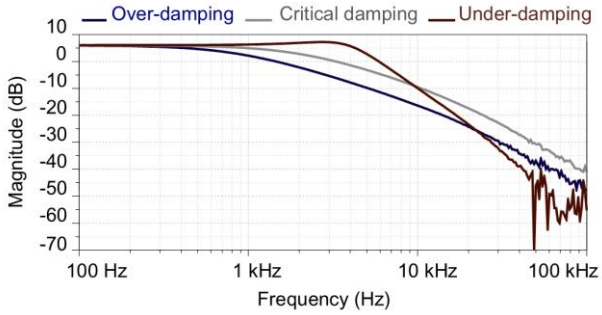


Fig. 31. Bode plot of the transfer function in the implemented circuit.

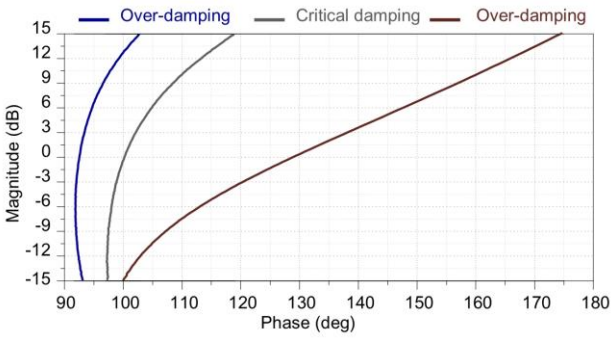


Fig. 32. Nichol plot of the self-loop function in the implemented circuit.

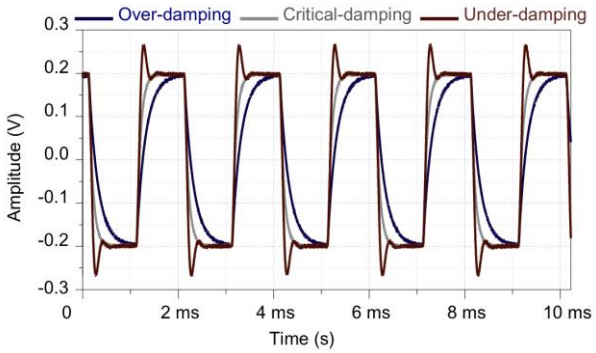


Fig. 33. Transient responses of the implemented circuit.

E. Ringing test for a fourth-order Rauch LPF

In this section, the operating regions of a fully differential 4th-order Rauch low-pass filter shall be analyzed. A differential form of the 4th-order Rauch low-pass filter is shown in Fig. 34. After applying the superposition principle at each node, the current node equations at nodes V_a, V_b, V_c, V_d, and V_e are derived in (42).

$$\begin{aligned}
&V_a\left(\frac{1}{R_1}+j\omega C_1+\frac{1}{R_2}+\frac{1}{R_3}\right)=\frac{V_{in}}{R_1}+\frac{V_b}{R_2}+\frac{(+j)^2V_c}{R_3}+(+j)^2V_a j\omega C_1;\\
&V_b\left(\frac{1}{R_2}+j\omega C_2\right)=\frac{V_a}{R_2}+(+j)^2V_c j\omega C_2;\ V_c=\left(V_b-(+j)^2V_b\right)A(\omega);\\
&V_d\left(\frac{1}{R_4}+j\omega C_3+\frac{1}{R_5}+\frac{1}{R_6}\right)=\frac{V_c}{R_4}+\frac{V_e}{R_5}+\frac{(+j)^2V_{out}}{R_6}+(+j)^2V_d j\omega C_3;\\
&V_e\left(\frac{1}{R_5}+j\omega C_4\right)=\frac{V_d}{R_5}+(+j)^2V_{out}j\omega C_4;\ V_{out}=\left(V_e-(+j)^2V_e\right)A(\omega);
\end{aligned} \tag{42}$$

Then, the open-loop function and the self-loop function of this op amp are given in (43). The values of the constant variables of the 4th-order fully differential Rauch low-pass filter are given in TABLE XI.

$$\begin{aligned}
&H(\omega)=\frac{b_0}{1+a_0(j\omega)^4+a_1(j\omega)^3+a_2(j\omega)^2+a_3 j\omega};\\
&L(\omega)=a_0(j\omega)^4+a_1(j\omega)^3+a_2(j\omega)^2+a_3 j\omega;
\end{aligned} \tag{43}$$

TABLE XI. VALUES OF GIVEN VARIABLES OF 4TH-ORDER RAUCH LPF.

Variable	Value
$\mathbf{b_0}$	$\frac{R_3R_6}{R_1R_4}$
$\mathbf{a_0}$	$R_2R_3R_5R_6C_1C_2C_3C_4$
$\mathbf{a_1}$	$R_2R_3\left(R_5+R_6+\frac{R_5R_6}{R_4}\right)C_1C_2C_4+R_5R_6\left(R_2+R_3+\frac{R_2R_3}{R_1}\right)C_2C_3C_4$
$\mathbf{a_2}$	$R_2R_3C_1C_2+R_5R_6C_3C_4+\left(R_2+R_3+\frac{R_2R_3}{R_1}\right)\left(R_5+R_6+\frac{R_5R_6}{R_4}\right)C_2C_4$
$\mathbf{a_3}$	$\left(R_2+R_3+\frac{R_2R_3}{R_1}\right)C_2+\left(R_5+R_6+\frac{R_5R_6}{R_4}\right)C_4$

The behaviors of the open loop function are shown in the previous section. The fully differential Rauch low-pass filter is designed for cut-off frequency f_0 = 100 kHz. Various values of capacitor C_1 were used to change the operating region of this filter. The entire device parameters of this filter are summarized in TABLE XII. To derive the self-loop function in high-order systems, the proposed comparison measurement and the alternating current conservation methods were introduced [44]. The Bode plot of the transfer function, the Nichols plot of the self-loop function, and transient response of the fully differential 4th-order Rauch low-pass filter are shown in Fig. 35. The simulation results of the self-loop function show that

- In the over-damping region, the phase margin is 74 degrees (observed at 106 degrees),
- In the critical damping region, the phase margin is 68 degrees (observed at 112 degrees), and
- In the under-damping region, the phase margin is 59 degrees (observed at 121 degrees); and the ringing occurs in the transient response of the under-damping region.

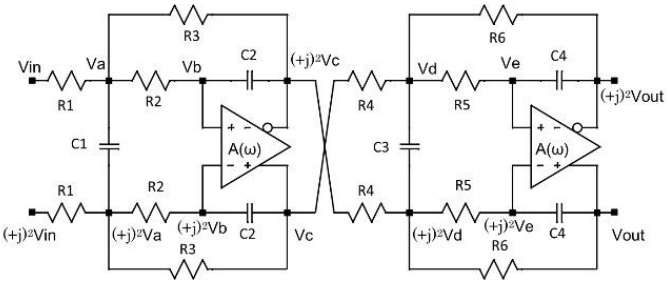


Fig. 34. Schematic diagram of a fully differential 4th-order Rauch LPF.

TABLE XII. DEVICE PARAMETERS OF 4TH-ORDER RAUCH LPF.

Element	Value	Element	Value	Element	Value
R_1	**1 kΩ**	**R_3**	**3 kΩ**	**R_5**	**1 kΩ**
R_2	**1 kΩ**	**R_4**	**2 kΩ**	**R_6**	**4 kΩ**
C_1	**0.4 nF**	**C_2**	**0.2 nF**	**C_4**	**0.3 nF**
Over-damping		**Critical damping**		**Under-damping**	
Element	**Value**	**Element**	**Value**	**Element**	**Value**
C_3	**0.1 nF**	**C_3**	**0.5 nF**	**C_3**	**1.4 nF**

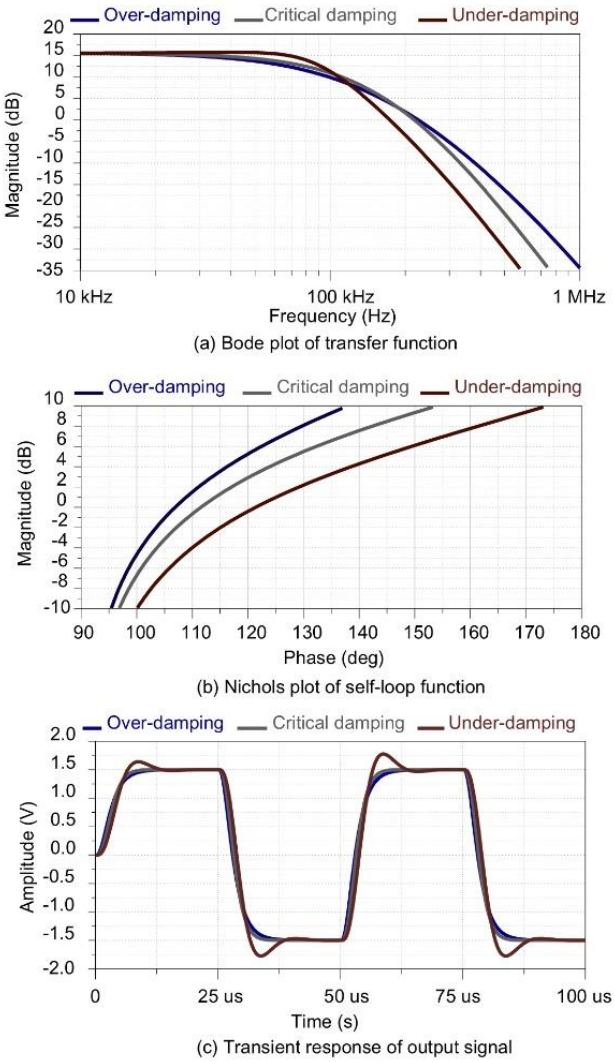


Fig. 35. Simulation results of the 4th-order Rauch low-pass filter.

It is emphasized that the Nyquist criterion for adaptive feedback systems can be only used to verify if the transfer function of a closed-loop system and the loop gain are well defined. Numerous research papers have demonstrated that the design procedure used in feedback control theory does indeed lead to a stable design and even to robust stability in the case of uncertain plants. However, a rigorous proof for the stability test based on Nichols chart of loop gain has not been formulated. The Nichols plot of a loop gain is very complicated. In this work, the Nichols plot of the self-loop function is easier than the conventional one as shown in Fig. 35(b). The phase margin of the self-loop function indicates the operating region of a linear network. In addition, the operating region of a general transfer function can be theoretically defined based on Pascal's triangle [45]. In the next section, the behaviors of a 4th-order Rauch complex filter will be analyzed.

VI. Models of High-Order Complex Filters

A. Design principle for active complex filter networks

The design principle for active complex filters is reviewed in this section. The transfer function and the image rejection ratio in the complex filters are not well defined in details. In recent years, the demand for fully integrated radio frequency transceivers in wireless communication gives rise to great attention to single chip low power transceivers [46]. Therefore, polyphase filters and complex filters are widely used in these transceivers. A complex filter is designed based on the frequency shifting of a real active low-pass filter as shown in Fig. 36. The transfer function of this complex filter is defined in (44). Here, ω_{cr} and ω_{cut} are cross and cut-off angular frequency [47].

$$H_{LPF}(\omega)=\frac{-A}{\left(j\frac{\omega}{\omega_{cut}}+1\right)} \xrightarrow{\omega-\omega_{cr}} H_{CF}(\omega)=\frac{-A}{\left(j\frac{\omega-\omega_{cr}}{\omega_{cut}}+1\right)} \tag{44}$$

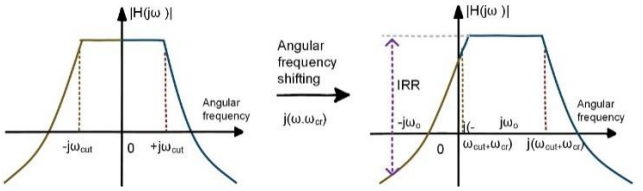


Fig. 36. Frequency shifting principle from a LPF into a complex filter.

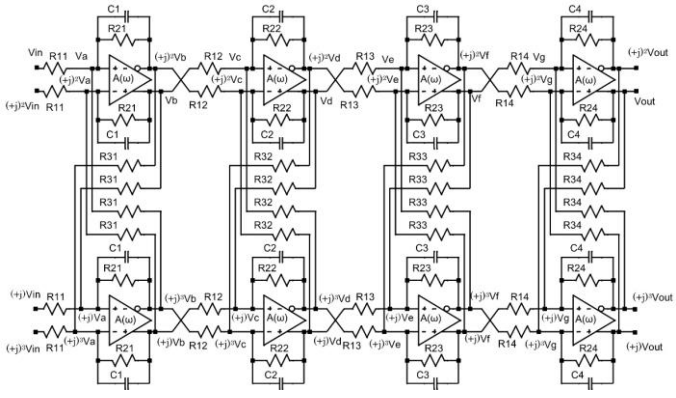


Fig. 37. Schematic of the 4th-order complex filter.

TABLE XIII. Values of Given Variables of Rauch Complex Filter.

Variable	Value
$\mathbf{b_0}$	$\frac{R_{21}}{R_{11}}\frac{R_{22}}{R_{12}}\frac{R_{23}}{R_{13}}\frac{R_{24}}{R_{14}}$
$\mathbf{a_0}$	$R_{21}R_{22}R_{23}R_{24}C_1C_2C_3C_4$
$\mathbf{a_{1P}}$	$R_{21}R_{22}C_1C_2\left(R_{23}C_3+R_{24}C_4\right)+R_{23}R_{24}C_3C_4\left(R_{21}C_1+R_{22}C_2\right)$ $+j\left[R_{21}R_{22}C_1C_2\left(\frac{R_{24}}{R_{34}}R_{23}C_3+\frac{R_{23}}{R_{33}}R_{24}C_4\right)+R_{23}R_{24}C_3C_4\left(\frac{R_{22}}{R_{32}}R_{21}C_1+\frac{R_{21}}{R_{31}}R_{22}C_2\right)\right]$
$\mathbf{a_{2P}}$	$R_{21}C_1\left(R_{22}C_2+R_{23}C_3+R_{24}C_4\right)+R_{22}C_2\left(R_{23}C_3+R_{24}C_4\right)+R_{23}R_{24}C_3C_4$ $+jR_{21}C_1\left[R_{22}C_2\left(\frac{R_{23}}{R_{33}}+\frac{R_{24}}{R_{34}}\right)+R_{23}C_3\left(\frac{R_{22}}{R_{32}}+\frac{R_{24}}{R_{34}}\right)+R_{24}C_4\left(\frac{R_{22}}{R_{32}}+\frac{R_{23}}{R_{33}}\right)\right]$ $+jR_{22}C_2\left[R_{23}C_3\left(\frac{R_{21}}{R_{31}}+\frac{R_{24}}{R_{34}}\right)+R_{24}C_4\left(\frac{R_{21}}{R_{31}}+\frac{R_{23}}{R_{33}}\right)\right]+jR_{23}R_{24}C_3C_4\left(\frac{R_{21}}{R_{31}}+\frac{R_{22}}{R_{32}}\right)$ $+(+j)^2R_{21}C_1\left(R_{22}C_2\frac{R_{23}}{R_{33}}\frac{R_{24}}{R_{34}}+R_{23}C_3\frac{R_{22}}{R_{32}}\frac{R_{24}}{R_{34}}+R_{24}C_4\frac{R_{22}}{R_{32}}\frac{R_{23}}{R_{33}}\right)$ $+(+j)^2\left[R_{22}C_2\left(R_{23}C_3\frac{R_{21}}{R_{31}}\frac{R_{24}}{R_{34}}+R_{24}C_4\frac{R_{23}}{R_{33}}\frac{R_{21}}{R_{31}}\right)+R_{23}R_{24}C_3C_4\frac{R_{21}}{R_{31}}\frac{R_{22}}{R_{32}}\right]$
$\mathbf{a_{3P}}$	$(+j)^3\left[R_{21}C_1\frac{R_{22}}{R_{32}}\frac{R_{23}}{R_{33}}\frac{R_{24}}{R_{34}}+R_{22}C_2\frac{R_{21}}{R_{31}}\frac{R_{23}}{R_{33}}\frac{R_{24}}{R_{34}}+R_{23}C_3\frac{R_{24}}{R_{34}}\frac{R_{21}}{R_{31}}\frac{R_{22}}{R_{32}}+R_{24}C_4\frac{R_{23}}{R_{33}}\frac{R_{21}}{R_{31}}\frac{R_{22}}{R_{32}}\right]$ $+R_{21}C_1+R_{22}C_2+(+j)^2\left[R_{21}C_1\left(\frac{R_{23}}{R_{33}}\frac{R_{24}}{R_{34}}+\frac{R_{22}}{R_{32}}\frac{R_{23}}{R_{33}}+\frac{R_{22}}{R_{32}}\frac{R_{24}}{R_{34}}\right)+R_{22}C_2\left(\frac{R_{23}}{R_{33}}\frac{R_{24}}{R_{34}}+\frac{R_{21}}{R_{31}}\frac{R_{23}}{R_{33}}+\frac{R_{21}}{R_{31}}\frac{R_{24}}{R_{34}}\right)\right]$ $+R_{23}C_3+R_{24}C_4+(+j)^2\left[R_{23}C_3\left(\frac{R_{21}}{R_{31}}\frac{R_{22}}{R_{32}}+\frac{R_{24}}{R_{34}}\frac{R_{21}}{R_{31}}+\frac{R_{24}}{R_{34}}\frac{R_{22}}{R_{32}}\right)+R_{24}C_4\left(\frac{R_{21}}{R_{31}}\frac{R_{22}}{R_{32}}+\frac{R_{23}}{R_{33}}\frac{R_{21}}{R_{31}}+\frac{R_{23}}{R_{33}}\frac{R_{22}}{R_{32}}\right)\right]$ $+j\left[R_{21}C_1\left(\frac{R_{23}}{R_{33}}+\frac{R_{24}}{R_{34}}+\frac{R_{22}}{R_{32}}\right)+R_{22}C_2\left(\frac{R_{23}}{R_{33}}+\frac{R_{24}}{R_{34}}+\frac{R_{21}}{R_{31}}\right)+R_{23}C_3\left(\frac{R_{21}}{R_{31}}+\frac{R_{22}}{R_{32}}+\frac{R_{24}}{R_{34}}\right)+R_{24}C_4\left(\frac{R_{21}}{R_{31}}+\frac{R_{22}}{R_{32}}+\frac{R_{23}}{R_{33}}\right)\right]$
$\mathbf{a_{4P}}$	$(+j)^4\frac{R_{21}}{R_{31}}\frac{R_{22}}{R_{32}}\frac{R_{23}}{R_{33}}\frac{R_{24}}{R_{34}}+(+j)^2\left[\frac{R_{21}}{R_{31}}\left(\frac{R_{22}}{R_{32}}+\frac{R_{23}}{R_{33}}+\frac{R_{24}}{R_{34}}\right)+\frac{R_{22}}{R_{32}}\left(\frac{R_{23}}{R_{33}}+\frac{R_{24}}{R_{34}}\right)+\frac{R_{23}}{R_{33}}\frac{R_{24}}{R_{34}}\right]$ $+(+j)^3\left[\frac{R_{21}}{R_{31}}\frac{R_{22}}{R_{32}}\left(\frac{R_{23}}{R_{33}}+\frac{R_{24}}{R_{34}}\right)+\frac{R_{23}}{R_{33}}\frac{R_{24}}{R_{34}}\left(\frac{R_{21}}{R_{31}}+\frac{R_{22}}{R_{32}}\right)\right]+j\left[\frac{R_{21}}{R_{31}}+\frac{R_{22}}{R_{32}}+\frac{R_{23}}{R_{33}}+\frac{R_{24}}{R_{34}}\right]$
$\mathbf{a_{1N}}$	$R_{21}R_{22}C_1C_2\left(R_{23}C_3+R_{24}C_4\right)+R_{23}R_{24}C_3C_4\left(R_{21}C_1+R_{22}C_2\right)$ $-j\left[R_{21}R_{22}C_1C_2\left(\frac{R_{24}}{R_{34}}R_{23}C_3+\frac{R_{23}}{R_{33}}R_{24}C_4\right)+R_{23}R_{24}C_3C_4\left(\frac{R_{22}}{R_{32}}R_{21}C_1+\frac{R_{21}}{R_{31}}R_{22}C_2\right)\right]$
$\mathbf{a_{2N}}$	$R_{21}C_1\left(R_{22}C_2+R_{23}C_3+R_{24}C_4\right)+R_{22}C_2\left(R_{23}C_3+R_{24}C_4\right)+R_{23}R_{24}C_3C_4$ $-jR_{21}C_1\left[R_{22}C_2\left(\frac{R_{23}}{R_{33}}+\frac{R_{24}}{R_{34}}\right)+R_{23}C_3\left(\frac{R_{22}}{R_{32}}+\frac{R_{24}}{R_{34}}\right)+R_{24}C_4\left(\frac{R_{22}}{R_{32}}+\frac{R_{23}}{R_{33}}\right)\right]$ $-jR_{22}C_2\left[R_{23}C_3\left(\frac{R_{21}}{R_{31}}+\frac{R_{24}}{R_{34}}\right)+R_{24}C_4\left(\frac{R_{21}}{R_{31}}+\frac{R_{23}}{R_{33}}\right)\right]+jR_{23}R_{24}C_3C_4\left(\frac{R_{21}}{R_{31}}+\frac{R_{22}}{R_{32}}\right)$ $+(-j)^2R_{21}C_1\left(R_{22}C_2\frac{R_{23}}{R_{33}}\frac{R_{24}}{R_{34}}+R_{23}C_3\frac{R_{22}}{R_{32}}\frac{R_{24}}{R_{34}}+R_{24}C_4\frac{R_{22}}{R_{32}}\frac{R_{23}}{R_{33}}\right)$ $+(-j)^2\left[R_{22}C_2\left(R_{23}C_3\frac{R_{21}}{R_{31}}\frac{R_{24}}{R_{34}}+R_{24}C_4\frac{R_{23}}{R_{33}}\frac{R_{21}}{R_{31}}\right)+R_{23}R_{24}C_3C_4\frac{R_{21}}{R_{31}}\frac{R_{22}}{R_{32}}\right]$
$\mathbf{a_{3N}}$	$(-j)^3\left[R_{21}C_1\frac{R_{22}}{R_{32}}\frac{R_{23}}{R_{33}}\frac{R_{24}}{R_{34}}+R_{22}C_2\frac{R_{21}}{R_{31}}\frac{R_{23}}{R_{33}}\frac{R_{24}}{R_{34}}+R_{23}C_3\frac{R_{24}}{R_{34}}\frac{R_{21}}{R_{31}}\frac{R_{22}}{R_{32}}+R_{24}C_4\frac{R_{23}}{R_{33}}\frac{R_{21}}{R_{31}}\frac{R_{22}}{R_{32}}\right]$ $+R_{21}C_1+R_{22}C_2+(-j)^2\left[R_{21}C_1\left(\frac{R_{23}}{R_{33}}\frac{R_{24}}{R_{34}}+\frac{R_{22}}{R_{32}}\frac{R_{23}}{R_{33}}+\frac{R_{22}}{R_{32}}\frac{R_{24}}{R_{34}}\right)+R_{22}C_2\left(\frac{R_{23}}{R_{33}}\frac{R_{24}}{R_{34}}+\frac{R_{21}}{R_{31}}\frac{R_{23}}{R_{33}}+\frac{R_{21}}{R_{31}}\frac{R_{24}}{R_{34}}\right)\right]$ $+R_{23}C_3+R_{24}C_4+(-j)^2\left[R_{23}C_3\left(\frac{R_{21}}{R_{31}}\frac{R_{22}}{R_{32}}+\frac{R_{24}}{R_{34}}\frac{R_{21}}{R_{31}}+\frac{R_{24}}{R_{34}}\frac{R_{22}}{R_{32}}\right)+R_{24}C_4\left(\frac{R_{21}}{R_{31}}\frac{R_{22}}{R_{32}}+\frac{R_{23}}{R_{33}}\frac{R_{21}}{R_{31}}+\frac{R_{23}}{R_{33}}\frac{R_{22}}{R_{32}}\right)\right]$ $-j\left[R_{21}C_1\left(\frac{R_{23}}{R_{33}}+\frac{R_{24}}{R_{34}}+\frac{R_{22}}{R_{32}}\right)+R_{22}C_2\left(\frac{R_{23}}{R_{33}}+\frac{R_{24}}{R_{34}}+\frac{R_{21}}{R_{31}}\right)+R_{23}C_3\left(\frac{R_{21}}{R_{31}}+\frac{R_{22}}{R_{32}}+\frac{R_{24}}{R_{34}}\right)+R_{24}C_4\left(\frac{R_{21}}{R_{31}}+\frac{R_{22}}{R_{32}}+\frac{R_{23}}{R_{33}}\right)\right]$
$\mathbf{a_{4N}}$	$(-j)^4\frac{R_{21}}{R_{31}}\frac{R_{22}}{R_{32}}\frac{R_{23}}{R_{33}}\frac{R_{24}}{R_{34}}+(-j)^2\left[\frac{R_{21}}{R_{31}}\left(\frac{R_{22}}{R_{32}}+\frac{R_{23}}{R_{33}}+\frac{R_{24}}{R_{34}}\right)+\frac{R_{22}}{R_{32}}\left(\frac{R_{23}}{R_{33}}+\frac{R_{24}}{R_{34}}\right)+\frac{R_{23}}{R_{33}}\frac{R_{24}}{R_{34}}\right]$ $+(-j)^3\left[\frac{R_{21}}{R_{31}}\frac{R_{22}}{R_{32}}\left(\frac{R_{23}}{R_{33}}+\frac{R_{24}}{R_{34}}\right)+\frac{R_{23}}{R_{33}}\frac{R_{24}}{R_{34}}\left(\frac{R_{21}}{R_{31}}+\frac{R_{22}}{R_{32}}\right)\right]-j\left[\frac{R_{21}}{R_{31}}+\frac{R_{22}}{R_{32}}+\frac{R_{23}}{R_{33}}+\frac{R_{24}}{R_{34}}\right]$

B. Behaviour of the conventional 4th-order complex filter

In this section, the behaviour of a 4th-order complex filter is reviewed. Fig. 37 shows the schematic diagram of the conventional 4th-order complex filter [48]. As the input signal sources are the positive polyphase signals $S_p\{V_1; V_2; V_3; V_4\}=\{1;(+j);(+j)^2;(+j)^3\}V(t)$, after the proposed superposition theorem is applied at each node, the current node equations at nodes V_a, V_b, V_c, V_d, V_e, V_f, V_g, and V_{out} are derived in (45).

$$V_a\left(\frac{1}{R_{11}}+\frac{1}{Z_{C1}}+\frac{1}{R_{21}}+\frac{1}{R_{31}}\right)=\frac{V_{in}}{R_{11}}+\frac{(+j)^3V_b}{R_{31}}+\left(\frac{1}{Z_{C1}}+\frac{1}{R_{21}}\right)(+j)^2V_b;$$
$$V_c\left(\frac{1}{R_{12}}+\frac{1}{Z_{C2}}+\frac{1}{R_{22}}+\frac{1}{R_{32}}\right)=\frac{V_b}{R_{12}}+\frac{(+j)^3V_d}{R_{31}}+\left(\frac{1}{Z_{C2}}+\frac{1}{R_{22}}\right)(+j)^2V_d; \quad (45)$$
$$V_b=\left[V_a-(+j)^2V_a\right]A(\omega);\ V_d=\left[V_c-(+j)^2V_c\right]A(\omega);$$
$$V_e\left(\frac{1}{R_{13}}+\frac{1}{Z_{C3}}+\frac{1}{R_{23}}+\frac{1}{R_{33}}\right)=\frac{V_d}{R_{13}}+\frac{(+j)^3V_f}{R_{33}}+\left(\frac{1}{Z_{C3}}+\frac{1}{R_{23}}\right)(+j)^2V_f;$$
$$V_g\left(\frac{1}{R_{14}}+\frac{1}{Z_{C4}}+\frac{1}{R_{24}}+\frac{1}{R_{34}}\right)=\frac{V_{in}}{R_{14}}+\frac{(+j)^3V_{out}}{R_{33}}+\left(\frac{1}{Z_{C4}}+\frac{1}{R_{24}}\right)(+j)^2V_{out};$$
$$V_f=\left[V_e-(+j)^2V_e\right]A(\omega);V_{out}=\left[V_g-(+j)^2V_g\right]A(\omega);$$

Then, the transfer function of this complex filter in the positive frequency domain is given in (46).

$$H_P(\omega)=\frac{b_0}{a_0(j\omega)^4+a_{1P}(j\omega)^3+a_{2P}(j\omega)^2+a_{3P}j\omega+a_{4P}+1}; \quad (46)$$

As the input sources are negative polyphase signals $S_n\{V_1; V_2; V_3; V_4\} = \{1; (-j); (-j)^2; (-j)^3\}$ V(t), the transfer function of the 4th-order complex filter in the negative frequency domain is given in (47).

$$H_N(\omega)=\frac{b_0}{a_0(j\omega)^4+a_{1N}(j\omega)^3+a_{2N}(j\omega)^2+a_{3N}j\omega+a_{4N}+1}; \quad (47)$$

Hence, the image rejection ratio of this complex filter is defined in (48). The values of the constant variables of the 4th-order complex filter are given in TABLE XIV.

$$IRR(\omega)=\frac{a_0(j\omega)^4+a_{1N}(j\omega)^3+a_{2N}(j\omega)^2+a_{3N}j\omega+a_{4N}+1}{a_0(j\omega)^4+a_{1P}(j\omega)^3+a_{2P}(j\omega)^2+a_{3P}j\omega+a_{4P}+1}; \quad (48)$$

TABLE XIV. DEVICE PARAMETERS OF COMPLEX FILTER.

Element	Value	Element	Value
R_{11}	2 kΩ	R_{12}	1 kΩ
R_{21}	7 kΩ	R_{22}	3.5 kΩ
R_{31}	2 kΩ	R_{32}	1 kΩ
C_1	86 pF	C_2	52 pF
R_{13}	2 kΩ	R_{14}	1 kΩ
R_{23}	7 kΩ	R_{24}	3.5 kΩ
R_{33}	2 kΩ	R_{34}	1 kΩ
C_3	86 pF	C_4	52 pF

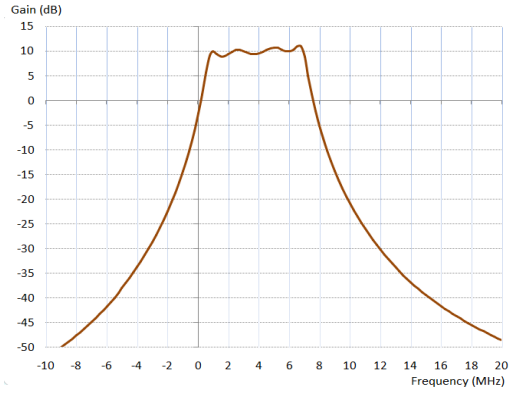


Fig. 38. Bode plot of the 4th-order complex filter.

Fig. 38 shows the behaviours of the 4th-order complex filter. In the positive frequency domain, the pass-band gain is 10 dB and the image signal rejection ratio is 33 dB.

C. Design of a 4th-order Rauch complex filter

In this section, a proposed design of a 4th-order Rauch complex filter is presented. The advantages of the Rauch architecture are an easier selection of circuit components and a simpler design in complex filters [49]. Fig. 39 shows the schematic diagram of a 4th-order Rauch complex filter. As the input signal sources are the positive polyphase signals $S_p\{V_1; V_2; V_3; V_4\}$, after the proposed superposition theorem is applied at each node, the current node equations at nodes V_a, V_b, V_c, V_d, V_e, and V_{out} are derived in (49).

$$V_a\left(\frac{1}{R_1}+j\omega C_1+\frac{1}{R_2}+\frac{1}{R_3}\right)=\frac{V_{in}}{R_1}+(+j)^2V_aj\omega C_1+\frac{V_b}{R_2}+\frac{(+j)^2V_c}{R_3};$$
$$V_b\left(\frac{1}{R_2}+j\omega C_2+\frac{1}{R_4}\right)=\frac{V_a}{R_2}+(+j)^2V_cj\omega C_2+\frac{(+j)^3V_c}{R_4}; \quad (49)$$
$$V_c=\left[V_b-(+j)^2V_b\right]A(\omega);V_{out}=\left[V_e-(+j)^2V_e\right]A(\omega);$$
$$V_d\left(\frac{1}{R_5}+j\omega C_3+\frac{1}{R_6}+\frac{1}{R_7}\right)=\frac{V_c}{R_5}+(+j)^2V_dj\omega C_3+\frac{V_e}{R_6}+\frac{(+j)^2V_{out}}{R_7};$$
$$V_e\left(\frac{1}{R_6}+j\omega C_4+\frac{1}{R_8}\right)=\frac{V_d}{R_6}+(+j)^2V_{out}j\omega C_4+\frac{(+j)^3V_{out}}{R_8};$$

Then, the transfer function of this complex filter in the positive frequency domain is given in (50).

$$H_P(\omega)=\frac{b_0}{a_0(j\omega)^4+a_{P1}(j\omega)^3+a_{P2}(j\omega)^2+a_{P3}j\omega+a_{P4}+1}; \quad (50)$$

As the input sources are negative polyphase signals $S_n\{V_1; V_2; V_3; V_4\}$, the transfer function of this complex filter in the negative frequency domain is given in (51).

$$H_N(\omega)=\frac{b_0}{a_0(j\omega)^4+a_{N1}(j\omega)^3+a_{N2}(j\omega)^2+a_{N3}j\omega+a_{N4}+1}; \quad (51)$$

Hence, the image rejection ratio of this complex filter is defined in (52). The values of the constant variables of the 4th-order Rauch complex filter are given in TABLE XV.

$$IRR(\omega)=\frac{a_0(j\omega)^4+a_{N1}(j\omega)^3+a_{N2}(j\omega)^2+a_{N3}j\omega+a_{N4}+1}{a_0(j\omega)^4+a_{P1}(j\omega)^3+a_{P2}(j\omega)^2+a_{P3}j\omega+a_{P4}+1}; \quad (52)$$

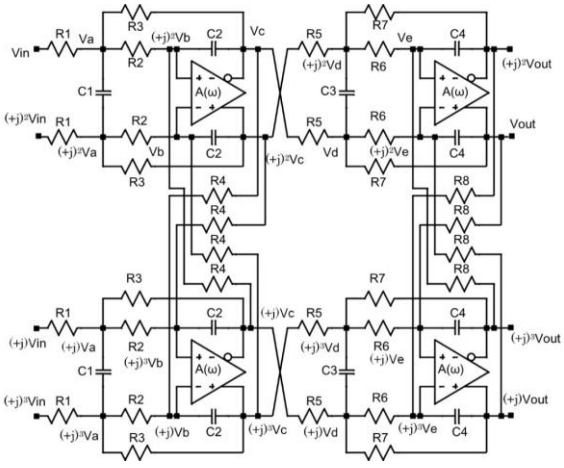


Fig. 39. Schematic of a 4th-order Rauch complex filter.

TABLE XV. VALUES OF GIVEN VARIABLES OF RAUCH COMPLEX FILTER.

Variable	Value
$\mathbf{b_0}$	$\frac{R_3}{R_1}\frac{R_7}{R_5}$
$\mathbf{a_0}$	$4R_2R_3R_6R_7C_1C_2C_3C_4$
$\mathbf{a_{P1}}$	$2R_2R_3C_1C_2C_4\left(R_6+R_7+\frac{R_6R_7}{R_5}\right)+2R_6R_7C_2C_3C_4\left(R_2+R_3+\frac{R_2R_3}{R_1}\right)+j2R_2R_3R_6R_7C_1C_3\left(\frac{C_2}{R_8}+\frac{C_4}{R_4}\right)$
$\mathbf{a_{P2}}$	$\frac{(+j)^2R_2R_3R_6R_7C_1C_3}{R_4R_8}+\left(R_2+R_3+\frac{R_2R_3}{R_1}\right)\left(R_6+R_7+\frac{R_6R_7}{R_5}\right)C_2C_4+2R_2R_3C_1C_2+2R_6R_7C_3C_4$ $+j\left[R_2R_3C_1\left(R_6+R_7+\frac{R_6R_7}{R_5}\right)\left(\frac{C_4}{R_4}+\frac{2C_2}{R_8}\right)+R_6R_7C_3\left(R_2+R_3+\frac{R_2R_3}{R_1}\right)\left(\frac{C_2}{R_8}+\frac{2C_4}{R_4}\right)\right]$
$\mathbf{a_{P3}}$	$\frac{(+j)^2}{R_4R_8}\left[\left(R_2+R_3+\frac{R_2R_3}{R_1}\right)R_6R_7C_3+\left(R_6+R_7+\frac{R_6R_7}{R_5}\right)R_2R_3C_1\right]+\left(R_2+R_3+\frac{R_2R_3}{R_1}\right)C_2+\left(R_6+R_7+\frac{R_6R_7}{R_5}\right)C_4$ $+j\left[\left(R_2+R_3+\frac{R_2R_3}{R_1}\right)\left(R_6+R_7+\frac{R_6R_7}{R_5}\right)\left(\frac{C_2}{R_8}+\frac{C_4}{R_4}\right)+\frac{R_2R_3C_1}{R_4}+\frac{R_6R_7C_3}{R_8}\right]$
$\mathbf{a_{P4}}$	$\frac{(+j)^2}{R_4R_8}\left(R_2+R_3+\frac{R_2R_3}{R_1}\right)\left(R_6+R_7+\frac{R_6R_7}{R_5}\right)+j\left[\left(R_2+R_3+\frac{R_2R_3}{R_1}\right)\frac{1}{R_4}+\left(R_6+R_7+\frac{R_6R_7}{R_5}\right)\frac{1}{R_8}\right]$
$\mathbf{a_{N1}}$	$2R_2R_3C_1C_2C_4\left(R_6+R_7+\frac{R_6R_7}{R_5}\right)+2R_6R_7C_2C_3C_4\left(R_2+R_3+\frac{R_2R_3}{R_1}\right)-j2R_2R_3R_6R_7C_1C_3\left(\frac{C_2}{R_8}+\frac{C_4}{R_4}\right)$
$\mathbf{a_{N2}}$	$\frac{(-j)^2R_2R_3R_6R_7C_1C_3}{R_4R_8}+\left(R_2+R_3+\frac{R_2R_3}{R_1}\right)\left(R_6+R_7+\frac{R_6R_7}{R_5}\right)C_2C_4+2R_2R_3C_1C_2+2R_6R_7C_3C_4$ $-j\left[R_2R_3C_1\left(R_6+R_7+\frac{R_6R_7}{R_5}\right)\left(\frac{C_4}{R_4}+\frac{2C_2}{R_8}\right)+R_6R_7C_3\left(R_2+R_3+\frac{R_2R_3}{R_1}\right)\left(\frac{C_2}{R_8}+\frac{2C_4}{R_4}\right)\right]$
$\mathbf{a_{N3}}$	$\frac{(-j)^2}{R_4R_8}\left[\left(R_2+R_3+\frac{R_2R_3}{R_1}\right)R_6R_7C_3+\left(R_6+R_7+\frac{R_6R_7}{R_5}\right)R_2R_3C_1\right]+\left(R_2+R_3+\frac{R_2R_3}{R_1}\right)C_2+\left(R_6+R_7+\frac{R_6R_7}{R_5}\right)C_4$ $-j\left[\left(R_2+R_3+\frac{R_2R_3}{R_1}\right)\left(R_6+R_7+\frac{R_6R_7}{R_5}\right)\left(\frac{C_2}{R_8}+\frac{C_4}{R_4}\right)+\frac{R_2R_3C_1}{R_4}+\frac{R_6R_7C_3}{R_8}\right]$
$\mathbf{a_{N4}}$	$\frac{(-j)^2}{R_4R_8}\left(R_2+R_3+\frac{R_2R_3}{R_1}\right)\left(R_6+R_7+\frac{R_6R_7}{R_5}\right)-j\left[\left(R_2+R_3+\frac{R_2R_3}{R_1}\right)\frac{1}{R_4}+\left(R_6+R_7+\frac{R_6R_7}{R_5}\right)\frac{1}{R_8}\right]$

TABLE XVI. DEVICE PARAMETERS OF RAUCH COMPLEX FILTER.

Element	Value	Element	Value
$\mathbf{R_1}$	**1 kΩ**	$\mathbf{R_4}$	**3 kΩ**
$\mathbf{R_2}$	**1 kΩ**	$\mathbf{C_1}$	**0.55 nF**
$\mathbf{R_3}$	**2.8 kΩ**	$\mathbf{C_2}$	**0.35 nF**
$\mathbf{R_5}$	**2 kΩ**	$\mathbf{R_8}$	**3 kΩ**
$\mathbf{R_6}$	**1 kΩ**	$\mathbf{C_3}$	**0.6 nF**
$\mathbf{R_7}$	**4 kΩ**	$\mathbf{C_4}$	**0.22 nF**

Values of the passive components of the 4th-order Rauch complex filter are chosen as shown in TABLE XVI. Fig. 40 shows the behaviors of the Rauch complex filter in both positive and negative frequency domains. In the positive frequency domain, the pass-band gain of this complex filter is 13 dB. The image signal rejection ratio of this complex filter is 32 dB. Compare the simulation results with mathematical analysis and other research papers, the properties of transfer functions are the same [50].

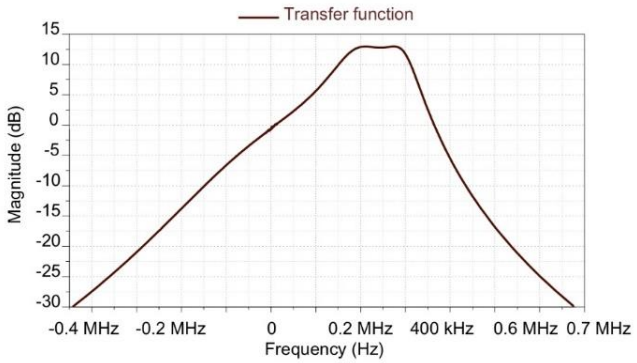


Fig. 40. Bode plot of the 4th-order Rauch complex filter.

VII. CONCLUSIONS

This paper has shown the analysis of complex functions in multi-source networks such as helix waves, polyphase signals, and high-order Rauch filters. The merits of Rauch filters are an easier selection of circuit components and a simpler design in fully differential forms. In complex functions, the imaginary unit j represents a 90-degree phase shift. A general superposition formula is proposed to analyse the behaviours of multi-source networks. This formula is considered as a fundamental concept for the theoretical multi-source network analysis because the effects of all the sources can be investigated at one time. The import of the superposition formula into the multi-source network analysis theory is relatively new with much recent progress regarding the circuit theory.

The ringing test for a fully differential 4th-order Rauch low-pass filter was performed based on the observation of the phase margin at unity gain of the self-loop function. The comparison measurement technique was used to measure the self-loop function in the transfer function of this low-pass filter. In case of under-damping, the magnitude of the transfer function is 15 dB and the phase margin is 59 degrees. Nichols chart of the self-loop function is considered as a practical tool for the stability test of electronic feedback systems. In future work, the ringing test for the parasitic components in the transmission lines, the printed circuit boards, and the physical layout layers will be done. A tool of the Nichols chart of self-loop function will be introduced.

This work also introduced a proposed design of a 4th-order Rauch complex filter. The image rejection ratio of this complex filter was also defined. The Bode plot of the Rauch complex filter was expressed in all frequency domains. The pass-band gain of this complex filter is 13 dB and the image signal rejection ratio is 32 dB. In future work, the effects of DC offsets and IQ mismatches in multi-source networks will be analyzed.

ACKNOWLEDGEMENTS

The authors would like to express their sincere gratitude to Prof. Hiroshi Tanimoto at Kitami Institute of Technology in Japan for his valuable comments.

REFERENCES

[1] M. Tran, A. Kuwana, H. Kobayashi, "Study of Rauch Low-Pass Filters using Pascal's Triangle", Int. Conf. on Elect., Info., & Com. (ICEIC 2021), Korea, Feb. 2021.

[2] I. Campanu, T. Salajan, R. Onet, M. Neag, "Comparative Analysis of Four Second-Order OA-RC Polyphase Filters for An ISM Low-IF Receiver," CAS 2012 Int. Semi. Conf., Romania, Oct. 2012.

[3] H. Kobayashi, M. Tran, K. Asami, A. Kuwana, H. San, "Complex Signal Processing in Analog / Mixed-Signal Circuits", 3rd Int. Conf. on Tech. & Soc. Sci. (ICTSS2019), Japan, May, 2019.

[4] M. Tran, Y. Sun, Y. Kobori, A. Kuwana, H. Kobayashi, "Design Proposal for Inductor Type Buck Converter in Bluetooth Receiver Chip with Overshoot Cancellation and Ripple Reduction Technique" Adv. Eng. For., vol. 38, pp.179-191, Nov. 2020.

[5] M. Tran, A. Hatta, A. Kuwana, H. Kobayashi, "Derivation of Image Rejection Ratio for High-Order Complex Filters," 6th Conf. on TJCAS, Nov. 2020.

[6] Y. Kobori, Y. Sun, M. Tran, A. Kuwana, H. Kobayashi, "EMI Reduction in Switching Converters with Pseudo Random Analog Noise", J. of Tech. & Soc. Sci., vol.4, no.2, pp.33-48, Apr. 2020.

[7] M. Tran, A. Kuwana, H. Kobayashi, "Study of Complex Functions in Multi-Source Networks", The 11th Annual Com. & Com. Work. & Conf. (IEEE CCWC 2021), USA, Jan. 2021.

Copyright © AJSE Publishers

[8] Y. Sun, Y. Kobori, M. Tran, A. Kuwana, H. Kobayashi, "Single-Inductor Dual-Output Converters With PWM, Hysteretic, Soft Switching and Current Controls", J. of Tech. & Soc. Sci., vol.4, no.2, pp.7-32, Apr. 2020.

[9] M. Tran, Y. Sun, N. Oiwa, Y. Kobori, A. Kuwana, H. Kobayashi, "Mathematical Analysis and Design of Parallel RLC Network in Step-down Switching Power Conversion System", J. of Mech. & Elect. Int. Sys., vol. 3, no. 2, May 2020.

[10] C. Zhang, Y. Sun, M. Tran, Y. Kobori, A. Kuwana, H. Kobayashi, "Multi-Phase Full/Half Wave Type Resonant Converters with Automatic Current Balance against Element Variation", 13th IEEE Int. Conf. on ASIC (ASICON 2019), Oct. 2019.

[11] M. Tran, A. Kuwana, H. Kobayashi, "Derivation of Loop Gain and Stability Test for Multiple Feedback Low Pass Filter Using Deboo Integrator", 8th IIAE Int. Conf. on Ind. App. Eng., Japan, March 2020.

[12] S. Delshadpour, "A 2.6 MHz Bandwidth, 3rd/5th Order Active-RC Polyphase Filter with Quadrature Offset Cancellation for Low-IF GPS Radio", 62nd Int. Mid. Symp. CAS, USA, Oct. 2019.

[13] M. Tran, A. Hatta, A. Kuwana, H. Kobayashi, "Design of 6th-Order Passive Quadrature Signal Generation Network Based on Polyphase Filter", IEEE 15th Int. Conf. on Solid-State & Integ. Cir. Tech. (ICSICT2020), China, Nov. 2020.

[14] A. Hatta, N. Kushita, M. Tran, K. Asami, A. Kuwana, H. Kobayashi, "Relationship Between Active Complex Bandpass Filter and Hilbert Filter" 5th Taiwan & Japan Conf. on CAS (TJCAS 2019), Aug. 2019.

[15] M. Tran, A. Kuwana, H. Kobayashi, "Design of Active Inductor and Stability Test for Ladder RLC Low Pass Filter Based on Widened Superposition and Voltage Injection", 8th IIAE Int. Conf. on Ind. App. Eng., Japan, March, 2020.

[16] M. Tran, A. Kuwana, H. Kobayashi "Ringing Test for Negative Feedback Amplifiers" 11th IEEE Annu. Inf. Tech., Elect. & Mob. Com. Conf. (IEMCON 2020), Canada, Nov. 2020.

[17] L. Severo, W. Noije, "A 0.4-V 10.9-µW/Pole 3rd-Order Complex BPF For Low Energy RF Receivers," IEEE Trans. CAS I, vol. 66, no. 6, pp. 2017–2026, 2019.

[18] M. Tran, A. Kuwana, H. Kobayashi, "Design of Active Inductor and Stability Test for Passive RLC Low Pass Filter", 10th Int. Conf. on Comp. Sci., Eng. & App. (CCSEA 2020), UK, Jul. 2020.

[19] Y. Kobori, J. Li, Y. Sun, M. Tran, A. Kuwana, H. Kobayashi, "Automatic Current Balance for Multi-Phase Switching Converters with Ripple Control or Soft Switch", Adv. Eng. For., vol. 38, pp.143-156, Nov. 2020.

[20] M. Tran, A. Kuwana, H. Kobayashi, "Derivation of Loop Gain and Stability Test for Low Pass Tow-Thomas Biquad Filter", 10th Int. Conf. on Comp. Sci., Eng. & App. (CCSEA 2020), UK, Jul. 2020.

[21] M. Tran, A. Kuwana, H. Kobayashi, "Ringing Test for Tow-Thomas Low-Pass Filters", Int. Conf. on Prom. Elect. Tech. (ICPET 2020), Palestine, 16-17, Dec. 2020.

[22] Y. Jou, H. Li, F. Chen, "Polyphase Design of 2-Channel Quadrature Mirror Filter Using Minor Component Analysis", IEEE 8th Global Conf. Consu. Elect., Japan, Oct. 2019.

[23] M. Tran, A. Kuwana, H. Kobayashi, "Study of Behaviors of Electronic Amplifiers using Nichols Chart", IEEE the 3rd Int. Conf. on Elect. & Com. Eng. (ICECE 2020), Xi'an, China, 14-16, Dec. 2020.

[24] Y. Kobori, Y. Sun, M. Tran, A. Kuwana, H. Kobayashi, "EMI Noise Reduction of DC-DC Switching Converters with Automatic Output Ripple Cancellation" Adv. Eng. For., vol. 38, pp.157-170, Nov. 2020.

[25] M. Tran, "Study of Multiphase Networks, Noise Reduction for DC-DC Converters, and Stability Test for Electronic Systems", ATS Doct. Dissert. Award Contest, 29th IEEE ATS, Malaysia, Nov. 2020.

[26] Y. Kobori, Y. Sun, M. Tran, A. Kuwana, H. Kobayashi, "Pulse Coding Controlled Switching Converter with Notch Frequency Generation in Noise Spectrum", Adv. Eng. For., vol. 38, pp.118-129, Nov. 2020.

[27] M. Tran, A. Kuwana, H. Kobayashi, "Ringing Test for 3rd-Order Ladder Low-Pass Filters", 11th IEEE Ann. Ubiq. Com., Elect. & Mob. Com. Conf. (UEMCON 2020), USA, Oct. 2020.

[28] Z. Xie, J. Wu, C. Chen,"A Compact Low-Power Biquad for Active-RC Complex Filter" IEEE Trans. CAS II, vol. 65, no. 6, pp. 709-713, 2018.

[29] M. Tran, A. Kuwana, H. Kobayashi, "Ringing Test for 2nd-Order Sallen-Key Low-Pass Filters", IEEE 2nd Int. Conf. on CAS (ICCS 2020), China, 10-13, Dec. 2020.

[30] S. Delshadpour, "A Low Power CMOS gm-C Polyphase Filter for Low-IF GPS Receiver", 25th IEEE Int. Conf. Elect., CAS, France, Jan. 2019.

[31] M. Tran, Y. Kobori, A. Kuwana, H. Kobayashi, "Phase Margin Test for Power-Stage of DC-DC Buck Converter", 4th Int. Conf. on Tech. & Soc. Sci. (ICTSS 2020), Japan, Dec. 2020.

[32] D. Maier, H. Brachtendorf, "Design of an active 2nd-order polyphase filter for image rejection in subsampling receivers", IEEE 28th Int. Conf. Radioelektronika, Czech Republic, Apr. 2018.

[33] M. Tran, A. Kuwana, H. Kobayashi, "Stability Test for High-Order Ladder Low-Pass Filters," 6th Conf. on TJCAS, Nov. 2020.

[34] M. Tran, Y. Kobori, A. Kuwana, H. Kobayashi, "Design of LC Harmonic Notch Filter for Ripple Reduction in Step-Down DC-DC Buck Converter", IEEE 15th Int. Conf. on Solid-State & Integ. Cir. Tech. (ICSSICT2020), China, Nov. 2020.

[35] M. Tran, N. Kushita, A. Kuwana, H. Kobayashi, "Mathematical Analysis and Design of 4-Stage Passive RC Network in RF Front-End System", 3rd Int. Conf. on Tech. & Soc. Sci. (ICTSS 2019), Japan, May, 2019.

[36] Y. Sun, M. Tran, Y. Kobori, A. Kuwana, H. Kobayashi, "EMI Noise Reduction and Output Ripple Cancellation for Full-Wave Type Soft-Switching Converter", 13th IEEE Int. Conf. on ASICON, Oct. 2019.

[37] M. Tran, A. Kuwana, H. Kobayashi, "Measurements of Self-loop Functions in High-order Passive and Active Low-Pass Filters," IEEE 15th Int. Conf. on Solid-State & Integ. Cir. Tech. (ICSICT2020), China, Nov. 2020.

[38] S. Katayama, J. Li, Y. Sun, M. Tran, Y. Kobori, A. Kuwana, H. Kobayashi, "Automatic Correction of Current Imbalance for Multi-Phase COT Ripple-Based Control DC-DC Converter", 13th IEEE Int. Conf. on ASICON, Oct. 2019.

[39] M. Tran, N. Kushita, A. Kuwana, H. Kobayashi, "Flat Pass-Band Method with Two RC Band-Stop Filters for 4-Stage Passive RC Polyphase Filter in Low-IF Receiver Systems", 3th IEEE Int. Conf. on ASICON, Oct. 2019.

[40] Y. Sun, M. Tran, Y. Kobori, A. Kuwana, H. Kobayashi, "Pulse Coding Control Switching Converter with Adjustable Conversion Voltage Ratio Notch Frequency Generation in Noise Spectrum", 13th IEEE Int. Conf. on ASICON, Oct. 2019.

[41] M. Tran, N. Kushita, A. Kuwana, H. Kobayashi, "Pass-band Gain Improvement Technique for Passive RC Polyphase Filter in Bluetooth Low-IF Receiver using Two RC Band-stop Filters", Advanced Engineering Forum, vol. 38, pp.192-205, Nov. 2020.

[42] Y. Kobori, N. Oiwa, S. Katayama, A. Bustoni, Y. Sun, M. Tran, A. Kuwana, H. Kobayashi, "EMI Reduction of PFC Rectifier and LLC Converter with Automatic Output Ripple Improvement", Adv. Eng. For., vol. 38, pp.103-117, Nov. 2020.

[43] M. Tran, Y. Sun, N. Oiwa, Y. Kobori, A. Kuwana, H. Kobayashi "Fast Response, Small Ripple, Low Noise Switching Converter with Digital Charge Time Control and EMI Harmonic Filter", J. of Mech. & Elect. Int. Sys., vol. 2, no. 1, pp.14-23, Dec. 2019.

[44] L. Severo, W. Noije, "A 10.9-µW/Pole 0.4-V Active-RC Complex BPF for Bluetooth Low Energy RF Receivers", IEEE 9th Latin Ame. Symp. CAS, Mexico, Feb. 2018.

[45] M. Tran, N. Kushita, A. Kuwana, H. Kobayashi, "Mathematical Model and Analysis of 4-Stage Passive RC Polyphase Filter for Low-IF Receiver", J. of Mech. & Elect. Int. Sys., vol. 3, no. 2, May 2020.

[46] K. Asami, N. Kushita, A. Hatta, M. Tran, Y. Tamura, A. Kuwana, H. Kobayashi, "I, Q Mismatch Analysis and Evaluation Method of Complex Analog Filter", 5th Conf. on TJCAS, Aug. 2019.

[47] H. Kobayashi, N. Kushita, M. Tran, K. Asami, H. San, A. Kuwana, "Analog / Mixed-Signal / RF Circuits for Complex Signal Processing", 13th IEEE Int. Conf. on ASICON, Oct. 2019.

[48] M. Tran, N. Kushita, A. Kuwana, H. Kobayashi, "Minimum Gain Ripple Technique for Pass-Band of 4-Stage Passive RC Polyphase Filter in Low IF Receivers", 5th Conf. on TJCAS, Aug. 2019.

[49] K. Asami, N. Kushita, A. Hatta, M. Tran, Y. Tamura, A. Kuwana, H. Kobayashi, "Analysis and Evaluation Method of RC Polyphase Filter", 13th IEEE Int. Conf. on ASICON, Oct. 2019.

[50] Y. Yin, S. Wang, Y. Ma, S. Kang, H. Guan, G. Jin, X. Qi, "The Design of Large Image Rejection and Wideband CMOS Active Polyphase Filter for BeiDou RF Receiver", IEICE Elec. Express, vol. 17, no. 12, 2020.

Copyright © AJSE Publishers